Published in final edited form as:
J Nonnewton Fluid Mech. 2008 October 1; 154(2-3): 120–135. doi:10.1016/j.jnnfm.2008.04.002.

Extensions of the Ferry shear wave model for active linear and nonlinear microrheology

Sorin M. Mitran, **M. Gregory Forest**, **Lingxing Yao**, **Brandon Lindley**[1], and **David B. Hill**[2]
The Virtual Lung Project, University of North Carolina, Chapel Hill, 27599-3250

[1]Applied Mathematics Program, Department of Mathematics, University of North Carolina, Chapel Hill, 27599-3250

[2]Cystic Fibrosis Center, University of North Carolina, Chapel Hill, 27599-7248

Abstract

The classical oscillatory shear wave model of Ferry *et al.* [J. Polym. Sci. 2:593-611, (1947)] is extended for active linear and nonlinear microrheology. In the Ferry protocol, oscillation and attenuation lengths of the shear wave measured from strobe photographs determine storage and loss moduli at each frequency of plate oscillation. The microliter volumes typical in biology require modifications of experimental method and theory. Microbead tracking replaces strobe photographs. Reflection from the top boundary yields counterpropagating modes which are modeled here for linear and nonlinear viscoelastic constitutive laws. Furthermore, bulk imposed strain is easily controlled, and we explore the onset of normal stress generation and shear thinning using nonlinear viscoelastic models. For this paper, we present the theory, exact linear and nonlinear solutions where possible, and simulation tools more generally. We then illustrate errors in inverse characterization by application of the Ferry formulas, due to both suppression of wave reflection and nonlinearity, even if there were no experimental error. This shear wave method presents an active and nonlinear analog of the two-point microrheology of Crocker *et al.* [Phys. Rev. Lett. 85: 888 - 891 (2000)]. Nonlocal (spatially extended) deformations and stresses are propagated through a small volume sample, on wavelengths long relative to bead size. The setup is ideal for exploration of nonlinear threshold behavior.

Keywords

Viscoelastic shear wave; Upper convected Maxwell model; Small sample effects; Biological fluids; Inverse characterization

1 Introduction

A classical [6,[8],[1]] method for linear viscoelastic characterization of gels and polymer solutions is based upon measurements of the unidirectional propagation of shear waves induced by an oscillating plate. The experimental technique and associated modeling and analysis are extensively discussed in the literature [30,[7],[2],[13],[14]]. Linear viscoelastic constitutive equations, coupled with momentum balance and boundary conditions, yield an exact solution for a semi-infinite domain. In the original method, strain-induced birefringence of synthetic polymers

allows visualization and strobe photography of the propagating shear wave. The measured shear wave oscillation and attenuation lengths are explicitly related to frequency-dependent shear and loss moduli. These formulas are recalled in Section 2.

Practical experimental apparatus of course uses a finite depth of fluid and shear waves reflect off the upper boundary. The effect of such reflections can be neglected as long as the exponential attenuation length of the shear wave is much shorter than the liquid layer depth; see [7], Chapter 5. The advantage of the Ferry design over various other devices carried over from acoustics, which involve interpreting surface signals, lies in the ability to strobe the entire shear wave as it progresses through the viscoelastic medium. The method is therefore effective *if* the material is birefringent under strain, and available in sufficient volumes. Linear response is ostensibly controlled in the bulk by imposing sufficiently small amplitude displacements, yet the possibility of large local strains near the source plate is evident even in the classical photographs.

When considering the problem of viscoelastic characterization of biological fluids, the hypotheses underlying the Ferry method break down. Typically, samples contain only a few microliters, and finite depth effects are important. Strobe photography is impractical. Nonlinear viscoelastic behavior is conjectured to have biological implications. Hence, a method to assess nonlinear effects is required.

Another implication of the inherent small length scales encountered in biology is that two different approaches to rheometry are possible. In classic rheometry at length scales much greater than microscopic free-path lengths, some sort of external forcing must be imposed on a fluid to study its response. However, at small length scales one can measure the response of a fluid to random thermal forcing, an approach known as *passive microrheometry*. Of course, the response to externally imposed forcing can also be studied and this is known as *active microrheometry*. Passive microrheometry must account for the stochastic forcing and also for the observation [4] that bulk behavior might not be correctly captured by techniques which use point measurements (e.g. single bead tracking techniques, [19]).

Our primary interest is the viscoelastic characterization of pulmonary liquids as part of the *Virtual Lung Project* at UNC Chapel Hill [31]. Hill and Superfine [11] have developed an active microrheometry technique based upon an oscillating plane Couette cell, similar in principle to the Ferry setup. Rather than rely upon visualization due to strain-induced birefringence, Hill and Superfine [11] mix micron-scale, neutrally buoyant beads and use particle-tracking to measure shear wave propagation features. This method is appealing for the following reasons.

- The setup mimics the *in vivo* conditions of oscillatory transport of pulmonary mucus by coordinated cilia and tidal breathing cycles. In Fig. 1 a schematic of the idealized biological configuration is presented in which multiple cilia beat in a coordinated fashion to impose an oscillatory motion at the bottom of a viscoelastic fluid layer. The more complicated geometry of the true biological system should not play a role in bulk viscoelastic characterization. Cilia are closely spaced on lung epithelial tissue with $\tilde{}0.5\,\mu m$ a typical distance between adjacent cilia, whereas the depth of the fluid layer is approximately $30\,\mu m$. At the low Reynolds numbers of interest, viscous effects rapidly smooth out the traces of excitation by individual cilia and the fluid appears as if put into motion by a flat plate.
- The bead position time series are dominated by non-local deformations and stresses rather than local thermal forcing of the bead by the fluid. The signals are deterministic rather than stochastic, and more accurately capture bulk behavior (similar to 2-point passive microrheology [4]). The viscoelastic response of the biological fluid can

exhibit scale-dependent behavior, but the Couette cell models the excitation of the entire depth of fluid by coordinated cilia beating, the normal mechanism for mucus transport.

- It is straightforward to include one-dimensional heterogeneity (stratification) effects both in the experiment and in the theoretical development presented below, enabling an experimental-modeling protocol for nonlinear inverse characterization at the low stress levels typical in human physiology.
- Both linear and nonlinear behavior can be investigated by controlling the lower plate oscillation amplitude. Shear thining and normal stress generation are phenomena specific to nonlinear viscoelastic fluids. We explore how to recognize the onset of nonlinear behavior as the plate-induced strain increases.

The modeling and assessment of counterpropagating waves and nonlinearity versus imposed strain, especially in regard to inverse characterization, are the primary contributions of this paper. We show in the present paper that accuracy of the classical Ferry formulas varies significantly depending on viscoelastic moduli versus frequency, imposed displacement amplitude, and sample height. For example, a conservative estimate of wave speeds for $30\mu m$ thick samples of a viscoelastic material, based on reported ranges of bulk moduli in pulmonary liquids, indicates multiple wave reflections *within* each period of plate oscillation in $10 - 20Hz$ frequency range. From simulated finite depth data for prescribed viscoelastic moduli, thereby removing any experimental error, we show that fitting to formulas based on unidirectional waves can lead to enormous errors in inverse recovery of the moduli.

The key issue motivating this paper is whether the assumptions of the Ferry model, linearity and a semi-infinite domain, are approximately satisfied under experimental conditions with limited volumes. More precisely, we assess accuracy of the linear, semi-infinite assumption across a multiple parameter space: storage and loss moduli versus frequency, gap height, and plate displacement amplitude. The infinite depth assumption is surely not valid, so the first target is to assess the order of errors in storage and loss moduli across some frequency range, due to this effect alone. Next, we aim to characterize the threshold strain (imposed by the lower plate displacement relative to sample height) at which nonlinear effects become significant, and to assess measurable flow and stress features triggered by nonlinearity. It is hypothesized that normal stresses in shear, a standard signature of nonlinearity, play an important role in pulmonary liquid transport by coordinated cilia and coughing events. A possible scenario is that normal and shear stresses propagate from the mucus and periciliary liquid layer to the epithelium, causing cellular compressive and shear strain, serving to regulate biochemical feedback. The role of shear thinning in pulmonary transport is not known, so a method is desirable that can simply ascertain whether a given sample shear thins under controlled strain conditions.

The remainder of this paper is organized as follows. Section 2 gives a summary of models, from linear–viscous to nonlinear–viscoelastic. Section 3 contains analytical results, including exact solutions and formulas for linear and nonlinear, semi-infinite and finite depth, models, as well as analysis of well-posed boundary conditions for the nonlinear models. Section 4 contains numerical studies of the two nonlinear models, their comparison to linear models and one other, and a discussion of physical predictions.

2 Shear wave models

2.1 Physical parameters and non-dimensionalization

We consider a layer of incompressible fluid of height $\tilde{H}$, set into motion by an oscillating lower flat plate, and whose upper surface remains flat and parallel to the lower plate. The $\tilde{}$ superscript

will be used to denote quantities expressed in physical units. The lower plate is set into harmonic motion $\tilde{V}(\tilde{t}) = \tilde{V}_0 \sin(\tilde{\omega}\tilde{t})$, as illustrated in Figure 1.

A reference viscosity $\tilde{\eta}_0$ value is chosen for the fluid of interest, namely the zero strain-rate viscosity of the fluid. The reference length $\tilde{A} = \tilde{V}_0/\tilde{\omega}$ is the maximum displacement of the driven plate; the reference time $\tilde{\omega}^{-1}$ is set by the plate frequency; and the reference stress $\tilde{\eta}_0\tilde{\omega}$ is the viscous plate shear stress. With this choice, the non-dimensional velocity of the lower plate is given by $v_x(0, t) = V(t) = \sin(t)$, where $v_x(y, t)$ denotes the velocity component of the fluid in the direction of plate motion at height y. It is a property of the model equations that with this scaling, we can focus on the 2-parameter space of values of storage and loss moduli, and make general statements about errors in recovering the moduli that depend only on the pair of values, independent of the imposed frequency. We return later to the practical implications of this scaling property. Let $\tilde{\lambda}$ be the relaxation time of the material. The following dimensionless parameters arise in the model equations:

- Reynolds number $Re = \tilde{\rho}\tilde{\omega}\tilde{A}^2/\tilde{\eta}_0$
- Deborah number $\lambda = \tilde{\lambda}\tilde{\omega}$
- Bulk shear strain $\gamma = \tilde{A}/\tilde{H}$.

2.2 Equations of motion

By symmetry, the one-dimensional propagation of velocity and stress leads to the following reductions in flow and stress variables, all functions only of t and the height y between the two flat surfaces. The fluid pressure p and velocity components are

$$p=p(y,t),\ v_x=v_x(y,t)v_y=0,\ v_z=0. \tag{1}$$

From $v_x(y, t)$, we may construct transient particle displacements $X(y, t)$ at each height (y) in the layer,

$$X(y,t)=\int_0^t v_x(y,t')\,dt'+X(y,0), \tag{2}$$

for given initial conditions $X(y, 0)$.

The fluid motion is determined from the non-dimensional momentum equation,

$$\frac{\partial v}{\partial t}+(v\cdot\nabla)v=\frac{1}{\mathrm{Re}}\nabla\cdot(-p\mathrm{I}+\tau), \tag{3}$$

together with a constitutive law for the extra stress, $\boldsymbol{\tau}$, which likewise is assumed to depend only on t and y,

$$\tau=\tau(y,t),\ \text{with}\ \tau_{xz}=\tau_{yz}=0. \tag{4}$$

To close the system for $(p, v_x, \boldsymbol{\tau})(y, t)$, we require the constitutive law relating $\boldsymbol{\tau}$ and $\nabla \boldsymbol{v}$. A hierarchy of laws has been discussed in standard texts [7], [2,[16]], the elements of which we now recall, mainly to present equations in the non-dimensional variables adopted here.

Newtonian Viscous Fluid—For viscous fluids, the Navier-Stokes constitutive law is $\tau_{xy} = \partial v_x/\partial y$ (the viscosity coefficient does not appear due to the scaling, 2.1) and the momentum equation (3) reduces to

$$\frac{\partial v_x}{\partial t} = \frac{1}{Re}\frac{\partial^2 v_x}{\partial y^2}, \frac{\partial p}{\partial y} = 0. \tag{5}$$

Linear Viscoelastic Fluids—The constitutive law of linear viscoelasticity (the Lodge model) is

$$\tau_{xy} = \int_{-\infty}^{t} G(t - t') \frac{\partial v_x}{\partial y}(y, t')\, dt', \tag{6}$$

where $G(t)$ is the non-dimensional shear relaxation modulus function. In physical units we have $\tilde{G} = \tilde{\eta}_0 \tilde{\omega} G$. The momentum equation (3) becomes

$$\frac{\partial v_x}{\partial t} = \frac{1}{Re}\int_{-\infty}^{t} G(t - t') \frac{\partial^2 v_x}{\partial y^2}(y, t')\, dt', \tag{7}$$

For a single-mode Maxwell fluid the shear modulus is $G(t) = (\eta_p/\lambda)\, e^{-t/\lambda}$ in non-dimensional form ($\eta_p = \tilde{\eta}_p/\tilde{\eta}_0$), and equation (7) simplifies to a damped wave (telegraphers) equation for v_x (cf. [7, [2]]),

$$\frac{\partial^2 v_x}{\partial t^2} - \frac{\eta_p}{\lambda Re}\frac{\partial^2 v_x}{\partial y^2} + \frac{1}{\lambda}\frac{\partial v_x}{\partial t} = 0. \tag{8}$$

Upper Convected Maxwell and Giesekus Models of Nonlinear Viscoelasticity— We consider nonlinear effects introduced by the upper convected derivative

$$\overset{\nabla}{\tau} = \frac{\partial \tau}{\partial t} + (v \cdot \nabla)\tau - (\nabla v)^T \tau - \tau(\nabla v), \tag{9}$$

and shear thining [2,[16]]. The constitutive relationship is a differential equation

$$\lambda \overset{\nabla}{\tau} = 2\eta_p \mathrm{D} - \tau - \alpha \tau \tau. \tag{10}$$

In this type of model the additional polymeric stress $\boldsymbol{\tau}$ is transported by the velocity field $\boldsymbol{v}$, decays exponentially at rate λ, is produced by the solvent fluid rate of strain

$D \equiv \frac{1}{2}\left(\nabla v + \nabla v^T\right)$ (non-dimensional), and is nonlinearly modified through the Giesekus term $(a/\lambda)\,\boldsymbol{\tau}\,\boldsymbol{\tau}$. The Giesekus "mobility parameter" a distinguishes various viscoelastic models: $a = 0$ reduces to the upper convected Maxwell (UCM) model, while $a = 0.5$ is the Leonov model. In general, it is assumed that $0 \leq a \leq 1$, and the mobility parameter is to be fitted from data along with λ.

The coupled system formed by the momentum and stress transport equations can be written as an evolution equation,

$$\frac{\partial q}{\partial t} + A(q)\frac{\partial q}{\partial y} = \psi(q), \tag{11}$$

with

$$q = \begin{bmatrix} v_x & \tau_{xx} & \tau_{xy} & \tau_{yy} \end{bmatrix}^T,$$

$$A(q) = -\begin{bmatrix} 0 & 0 & 1/Re & 0 \\ 2\tau_{xy} & 0 & 0 & 0 \\ \eta_p/\lambda + \tau_{yy} & 0 & 0 & 0 \\ 0 & 0 & 0 & 0 \end{bmatrix}, \psi = -\frac{1}{\lambda}\begin{bmatrix} 0 \\ \tau_{xx} + a\left(\tau_{xx}^2 + \tau_{xy}^2\right) \\ \tau_{xy} + a\,\tau_{xy}\left(\tau_{xx} + \tau_{yy}\right) \\ \tau_{yy} + a\left(\tau_{xy}^2 + \tau_{yy}^2\right) \end{bmatrix},$$

together with the pressure equation

$$\frac{\partial p}{\partial y} = \frac{\partial \tau_{yy}}{\partial y}. \tag{12}$$

As in the Newtonian fluid case, there is no convective nonlinearity in the momentum equation itself. An important indicator of nonlinearity is the shear-induced generation of a non-zero first normal stress difference, $N_1 = \tau_{xx} - \tau_{yy}$, an easily measured feature. The presence of a normal stress gradient along the y-direction then generates a pressure gradient, absent in the linear model. Indeed, neglecting all nonlinear terms from (equation 11) the two normal stress components τ_{xx}, τ_{yy}, obey identical ordinary differential equations

$$\frac{\partial \tau_{xx}}{\partial t} + \frac{1}{\lambda}\tau_{xx} = 0, \quad \frac{\partial \tau_{yy}}{\partial t} + \frac{1}{\lambda}\tau_{yy} = 0. \tag{13}$$

Thus, there is no possibility of generation of normal stresses in shear flow under linear assumptions. Additionally, any initial normal stresses distributed across the layer relax exponentially fast, and do not propagate nor couple to the shear stress and shear wave.

2.3 Boundary conditions

Boundary conditions are required at the lower plate $y = 0$, which is experimentally controlled, and at the top boundary $y = H$, which may or may not be explicitly controlled. The system of partial differential equations (equation 11) is hyperbolic if the normal stress τ_{yy} obeys an inequality (see Sect. 3.3.1). If the inequality is violated, the model is no longer well-posed for

the study of this experiment, a common occurrence for Maxwell-type models (cf. [9]). Hence, the characteristics of the system must be investigated to determine allowable boundary conditions. The following physically motivated conditions are analyzed in Sec. 3.3.2.

2.3.1 Lower plate boundary condition—At $y = 0$, no-slip boundary conditions apply, so that

$$v_x(y=0,t) = V(t), \tag{14}$$

with $V(t)$ the imposed velocity of the lower plate.

2.3.2 Top boundary condition—We distinguish two types of top (flat) interface conditions:

1. The top of the layer is in contact with a flat plate, which could be held stationary or driven at velocity $V_H(t)$

$$v_x(y=H,t) = V_H(t). \tag{15}$$

   The stationary upper plate condition is the most readily realized experimental condition when seeking inverse characterization.

2. The top of the layer is in contact with another fluid, in which case continuity of shear stress yields

$$\tau_{xy}(y=H,t) = \tau_{xy}(H,t) \text{ of the ambient fluid} \tag{16}$$

   The simplest case is to assume a passive ambient so that the shear stress is identically zero.

We address the issue of normal stress boundary conditions in the characteristic analysis below.

3 Analytical results

For viscous and linear viscoelastic fluids, with semi-infinite and finite domains, the model equations above are exactly solvable by Fourier methods if one ignores transients, and further solvable with transients by Laplace methods. The traditional approach (cf. Ferry [7]) is to suppress transients, leading to closed form solutions whose experimentally measurable features (e.g. attenuation length and shear wavelength) are explicitly related to material properties. Thus inverse characterization is given by simple formulas. We review these results now with some extensions that appear to be absent in the literature. The numerical solutions, naturally, can easily be used to model transients. We further show that the nonlinear model for an upper convected Maxwell law is also exactly solvable, and therefore explicit representations for normal stress generation in shear are determined. The Giesekus model does not submit to a closed-form solution.

3.1 Viscous fluid solution

The long-time solution for the viscous model (equation 5) is widely available (e.g. [27]) and recalled for completeness as well as comparison with generalizations.

Semi-infinite domain solution—Upon positing a solution of the form $v_x(y, t) = \mathcal{I}m\{\tilde{V}_x(y) e^{it}\}$ (recall time is measured in units of $\tilde{\omega}^{-1}$, so the physical frequency is $\tilde{\omega}/2\pi$), the solution is given by

$$v_x(y,t) = \mathcal{I}m\left\{e^{-\delta_0 y} e^{it}\right\} = e^{-\alpha_0 y}\sin(t-\beta_0 y),$$

which obeys the far-field boundary condition $\lim_{y\to\infty} v_x(y, t) = 0$. We have introduced $\delta_0=\alpha_0+i\beta_0= \sqrt{\mathrm{i\ Re}}= (1+i)\ \sqrt{Re/2}$. The Reynolds number, $Re = \tilde{\rho}\tilde{\omega}\tilde{A}^2/\tilde{\eta}_0$, determines both the penetration $(1/\alpha_0)$ and oscillation $(2\pi/\beta_0)$ lengthscales, through $\alpha_0=\beta_0= \sqrt{\mathrm{Re}/2}$. The velocity field produces a particle displacement

$$X(y,t) = X(y,0) + e^{-\alpha_0 y}\left[\cos(\beta t) - \cos(t-\beta y)\right]$$

The viscous shear stress is given by $\tau_{xy} = \partial v_x/\partial y$,

$$\tau_{xy}(y,t) = \mathcal{I}m\left\{-\delta_0 e^{-\delta_0 y} e^{it}\right\} = \sin(t-\beta_0 y+5\pi/4) e^{-\alpha_0 y}\sqrt{Re},$$

showing a constant phase difference $\varphi = 5\pi/4$ between the shear stress and the velocity.

Finite-depth channel with stationary upper plate—The no-slip boundary condition at the top of the channel reads $v_x(y = H, t) = 0$. The solution is simple to derive

$$v_x(y,t) = \mathcal{I}m\left\{e^{it}\frac{\sinh\left[\delta_0(H-y)\right]}{\sinh\left[\delta_0 H\right]}\right\}, \tag{17}$$

but does not appear to have been written down in the literature.

3.2 Linear viscoelastic model solutions

We summarize the Fourier, frequency-locked solutions to (equation 7) with the lower plate forcing $V(t) = \sin(t)$, ignoring transients.

Semi-infinite domain solution [7]—If the loss modulus is non-zero, then

$$v_x(y\to\infty, t) = 0. \tag{18}$$

A separable Fourier solution is posited, $v_x(y, t) = \mathcal{I}m\{\hat{v}_x(y)e^{it}\}$. Then from (equation 6) and (equation 7) a simple ordinary differential equation for $\hat{v}_x(y)$ is obtained,

$$\frac{d^2\widehat{v_x}}{\mathrm{d}y^2} - \frac{\mathrm{i\ Re}}{\eta^*}\widehat{v_x} = 0, \tag{19}$$

where the non-dimensional complex viscosity

$$\eta* = \int_0^\infty G(s) \exp(-is)\, ds = \eta' - i\eta'', \tag{20}$$

has been introduced. For a Maxwell model with $G(s) = (\eta_p/\lambda)e^{-s/\lambda}$ we obtain

$$\eta' = \frac{\eta_p}{1+\lambda^2}, \eta'' = \frac{\eta_p \lambda}{1+\lambda^2}. \tag{21}$$

The decay condition (equation 18) selects one independent solution of (equation 19), and the velocity has the same form as the viscous solution:

$$v_x(y,t) = \mathcal{I}m\left\{e^{it}e^{-\delta y}\right\} = e^{-\alpha y}\sin(t-\beta y), \tag{22}$$

where $\delta = \alpha + i\beta = \sqrt{i\,\mathrm{Re}/\eta*}$, $(a, \beta \in \mathbb{R}+)$,

$$\alpha = \frac{\sqrt{Re/2}}{|\eta*|}\sqrt{|\eta*| - \eta''},\ \beta = \sqrt{\frac{Re/2}{|\eta*|}}\sqrt{|\eta*| + \eta''}. \tag{23}$$

For the single mode Maxwell fluid

$$\alpha^2 = \frac{Re}{2}\frac{\sqrt{1+\lambda^2} - \lambda}{\eta_p} = \frac{1}{2c^2}\left(\sqrt{\frac{1}{\lambda^2}+1} - 1\right), \tag{24}$$

$$\beta^2 = \frac{Re}{2}\frac{\sqrt{1+\lambda^2} + \lambda}{\eta_p} = \frac{1}{2c^2}\left(\sqrt{\frac{1}{\lambda^2}+1} + 1\right), \tag{25}$$

where the "zero-stress" shear wave speed $c = \sqrt{\eta_p/(\lambda\,\mathrm{Re})}$ has been introduced. Clearly, $0 < \alpha \leq \beta$, with equality only in the viscous limit $\eta'' = 0$, $\eta* = 1$ ($\lambda = 0$, $\eta_p = 1$) such that $\alpha = \beta = \sqrt{Re/2}$. The greater the elastic component η'', the larger the difference between the oscillation wavelength $2\pi/\beta$ and the attenuation length $1/\alpha$.

The transform of the complex modulus, $G(\omega) = G' + iG''$, in our choice of non-dimensional units, is related to the complex viscosity $\eta(\omega)$ by $G = i\eta*$; in dimensional units, $\tilde{G} = i\tilde{\omega}\tilde{\eta}*$. The non-dimensional formulas relating storage and loss moduli and the reciprocal lengthscales α and β are:

$$G\prime=\frac{\left(\beta^2-\alpha^2\right)\mathrm{Re}}{\left(\alpha^2+\beta^2\right)^2},\ G''=\frac{2\alpha\beta\,\mathrm{Re}}{\left(\alpha^2+\beta^2\right)^2}. \tag{26}$$

Re-expressing the above formulas in physical quantities recovers the formulas of Ferry, Sawyer, and Ashworth [7]

$$\tilde{G\prime}=\tilde{\rho}\,\tilde{\omega}^2\frac{\left(\tilde{\beta}^2-\tilde{\alpha}^2\right)}{\left(\tilde{\alpha}^2+\tilde{\beta}^2\right)^2},\tilde{G''}=\tilde{\rho}\,\tilde{\omega}^2\frac{2\,\tilde{\alpha}\tilde{\beta}}{\left(\tilde{\alpha}^2+\tilde{\beta}^2\right)^2},$$

used to infer $\tilde{G'}(\omega)$, $\tilde{G''}(\omega)$ from experimental measurements of $\tilde{\alpha}=\alpha\tilde{A},\tilde{\beta}=\beta\tilde{A}$.

The particle positions $X(y, t)$ at height y are then given by

$$X(y,t)=X(y,0)+e^{-\alpha y}[\cos(\beta y)-\cos(t-\beta y)]. \tag{27}$$

The shear stress can be computed using the Lodge stress formula (equation 6)

$$\tau_{xy}(y,t)=\mathcal{I}m\left\{\int_{-\infty}^{t}G(t-t\prime)\frac{d\widehat{v_x}}{dy}(y)\,e^{it\prime}dt\prime\right\}=\mathcal{I}m\left\{\eta*\frac{d\widehat{v_x}}{dy}(y)\,e^{it}\right\}.$$

From the velocity (equation 22) we obtain,

$$\tau_{xy}(y,t)=\mathcal{I}m\left\{-\delta\eta*e^{it}e^{-\delta y}\right\}=\sin(t-\beta y+\varphi+\pi)\,e^{-\alpha y}\sqrt{|\eta*|\,Re}, \tag{28}$$

and, of course, the normal stresses are identically zero for linear viscoelasticity, $\tau_{xx}=\tau_{yy}=\tau_{zz}=0$. The phase shift of the tangential stress with respect to the velocity is $\varphi+\pi$, with $\varphi=\arctan(\beta/\alpha)$, $0\le\varphi\le\pi/2$. Note that the stress required to achieve the claimed boundary condition on plate speed is $\tau_{xy}(y=0,t)=-\sin(t+\varphi)\sqrt{|\eta*|\,Re}$.

A comparison to the viscous solution is informative. The ratio of the viscous to viscoelastic penetration lengths (α/α_0) is shown in Fig. 2. When $\eta''=0$ we obtain the expected increase in penetration depth as η' increases – a more viscous fluid leads to more momentum transfer from the oscillating plate. As the fluid elasticity η'' increases, the penetration depth ratio decreases. Some of the momentum imparted to the fluid by the oscillating plate is now radiated as an elastic shear wave, hence the penetration depth is smaller. The ratio of viscid to viscoelastic wavelengths (β/β_0) is also shown in Fig. 2. For viscoelastic fluids with $\eta''>0$ the wavelength reflects the competition between diffusive and radiative momentum transfer. At a given η' an initial increase in the elasticity decreases the wavelength. In this range the motion is overdamped and the decrease in penetration depth dominates the wavelength. At greater values of η'' the radiative momentum transfer (through shear waves) becomes dominant and there is

an increase in the wavelength. The maximum viscoelastic shear stress is greater than the purely viscous stress by a factor of $\sqrt{|\eta^*|}$ and exhibits a different phase shift, $\varphi + \pi$ instead of $5\pi/4$.

Finite channel depth—When the fluid is bounded above at $y = H$ by a flat interface moving at velocity $v_H(t)$, a no-slip boundary condition yields

$$v_x(y=H,t) = v_H(t).$$

The Fourier method used here ignores transients and can only be used for upper plate velocities of the form $v_H(t) = V_H e^{it}$ with V_H some complex constant giving the amplitude of the upper plate motion as well as its relative phase with respect to the lower plate forcing. The solution in this case is given by

$$v_x(y,t) = \mathcal{I}m\left\{e^{it}\frac{\sinh[\delta(H-y)]}{\sinh(\delta H)} + V_H e^{it}\frac{\sinh(\delta y)}{\sinh(\delta H)}\right\}. \tag{29}$$

The most easily controlled experimental condition is to place a stationary solid lid on the top interface in which case $V_H = 0$,

$$v_x(y,t) = \mathcal{I}m\left\{e^{it}\frac{\sinh[\delta(H-y)]}{\sinh(\delta H)}\right\}, \tag{30}$$

a simple formula which appears not to have been published before. It is the basis of the finite-depth inverse characterization presented below. The half-plane solution (equation 22) is recovered in the limit $H \to \infty$

$$\lim_{H\to\infty}\frac{\sinh[\delta(H-y)]}{\sinh(\delta H)} = e^{-\delta y},\quad \lim_{H\to\infty}\frac{\sinh(\delta y)}{\sinh(\delta H)} = 0, \tag{31}$$

recalling that $\delta = \alpha + i\beta$ and $\alpha > 0$. The stress is given by

$$\tau_{xy}(y,t) = \mathcal{I}m\left\{-\delta\eta^*\frac{\cosh[\delta(H-y)]}{\sinh(\delta H)}e^{it}\right\}.$$

Finite channel depth, flat fluid-fluid boundary above—The boundary condition in this case is continuity of tangential stress within the viscoelastic fluid $\tau_{yx}(H, t)$ and the adjacent fluid $\tau_H(t)$. Again, because we are neglecting transients, the adjacent fluid must exhibit a tangential stress dependence of the form $\tau_H(t) = T_H e^{it}$ to be consistent with the Fourier procedure. This leads to

$$\frac{dv_x^0}{dy}(y=H) = \frac{T_H}{\eta^*}, \tag{32}$$

and the solution

$$v_x(y,t) = \mathcal{I}m\left\{e^{it}\left[\frac{\cosh\left[\delta(H-y)\right]}{\cosh\left(\delta H\right)} + \frac{T_H}{\eta * \delta}\frac{\sinh(\delta y)}{\cosh(\delta H)}\right]\right\}. \tag{33}$$

This solution is relevant if one solves the model equations for the fluid layer above, or designs an experiment with a controlled dynamic shear stress at the interface.

It should be noted however that ensuring that the top fluid layer has the simple harmonic tangential stress $\tau_H(t) = T_H e^{it}$ is difficult to realize experimentally. If the adjacent fluid exerts negligible stress upon the viscoelastic fluid layer $T_H \cong 0$, then the formula

$$v_x(y,t) = \mathcal{I}m\left\{e^{it}\frac{\cosh\left[\delta(H-y)\right]}{\cosh\left(\delta H\right)}\right\},$$

is valid. Otherwise, it is to be expected that $\tau_H(t)$ contains other frequencies besides the fundamental frequency used in the lower plate forcing e^{it}. Should one attempt, irrespective of this observation, to use formula (equation 33), then the complex viscosity deduced from the experimental measurements will be affected by aliasing of the additional frequencies present in $\tau_H(t)$ onto the fundamental mode e^{it}.

Linear model limitations—The constitutive law (equation 6) is valid for small strains

$$\max\left|D_{xy}\right| = \max\left|\frac{\partial u}{\partial y}\right| = \max\left|\frac{\partial}{\partial y}\int_0^t v_x(y,s)\,ds\right| \ll 1.$$

For the half-plane solution (equation 22) the strain is given by

$$D_{xy}(y,t) = e^{-\alpha y}\left\{\alpha\left[\cos(t-\beta y) - \cos(\beta y)\right] + \beta\left[\sin(t-\beta y) + \sin(\beta y)\right]\right\},$$

assuming $X(y, 0) = 0$. Physically we expect the maximum strain to be obtained at $y = 0$ where the displacement is

$$X(y=0,t) = -\alpha(1-\cos t) - \beta\sin t.$$

The extremum of $X(0, t)$ is obtained when $(\cos t, \sin t) = (\alpha,\beta)/\sqrt{\alpha^2+\beta^2}$, hence

$$\max|D_{xy}| = \sqrt{\alpha^2+\beta^2} - \alpha.$$

Since $\sqrt{\alpha^2+\beta^2} = \sqrt{Re/|\eta*|}$, the small strain condition becomes

$$\sqrt{\frac{Re}{|\eta*|}}\left(1-\sqrt{\frac{|\eta*|-\eta''}{2\,|\eta*|}}\right)\ll 1.$$

The elastic limit of fluid behavior corresponds to $\eta'' \gg \eta'$ for which the small strain condition becomes

$$Re \ll \eta''.$$

It is useful to revert to physical units to highlight the significance of these limits. Recall that $Re = \tilde{\rho}\tilde{\omega}\tilde{A}^2/\tilde{\eta}_0$ and $\tilde{G}' = \tilde{\omega}\tilde{\eta}''$. The small strain condition in the elastic limit then states that

$$\tilde{\rho}\left(\tilde{\omega}\tilde{A}\right)^2 \ll \tilde{G}',$$

or, physically, that the dynamic pressure induced by the oscillating plate must be much less than the elastic modulus of the fluid. In the viscous limit $\eta' = 1$, $\eta'' = 0$, the small-strain condition becomes $\sqrt{Re} \ll 1$. In physical terms this states that

$$\tilde{A} \ll \sqrt{2\,\tilde{\nu}\,/\,\tilde{\omega}},$$

or that the amplitude $\tilde{A}$ of the oscillating lower plate must be much less than the viscous penetration depth $\sqrt{2\,\tilde{\nu}\,/\,\tilde{\omega}}$. If viscous and elastic effects are roughly equal, $\eta' \cong \eta''$, then the small strain condition becomes

$$\mathrm{Re} << \min(\eta', \eta'').$$

The coefficients (η', η'') obtained from fitting experimental data to the formulas above should be checked against these limits to ascertain whether non-linear effects are insignificant. In the finite-depth linear and nonlinear models, one can calculate the local strain from the numerical solutions, which generically will be maximal in the first half-wavelength of the shear deformation at the lower plate.

3.3 Nonlinear model solution in special limits

3.3.1 Hyperbolic system structure—We now turn to a consideration of nonlinear effects by solving (equation 11). If the system obeys the linear limit, that will become evident from the solution. Our focus is conditions where nonlinear effects are measurable. In general numerical methods are required for a solution. We present the analysis needed for such numerical methods. For the upper convected Maxwell model, quite conclusive analytical results are attainable.

The matrix $\boldsymbol{A}$ from (equation 11) has eigenvalues $\mu_1 = \mu_2 = 0$, $\mu_3 = -c$, $\mu_4 = c$ with

$$c=\sqrt{\eta_p/(\lambda \mathrm{Re})+\tau_{yy}/\mathrm{Re}}, \tag{34}$$

denoting the velocity of propagation of shear waves transverse to the flow direction. If the fluid is elastic to some extent, then $\lambda > 0$ and finite. Furthermore if $\tau_{yy} \geq 0$ then the shear wave velocity c is a real number. It is interesting to note that for a given relaxation time λ there exists a critical normal stress $\tau_{yy} = -\eta_p/\lambda$ at which $c = 0$, and for $\tau_{yy} < -\eta_p/\lambda$, the system is no longer hyperbolic, but elliptic. The associated right eigenvectors are

$$R=[r_1 \quad r_2 \quad r_3 \quad r_4]=\begin{bmatrix} 0 & 0 & -c & c \\ 0 & 1 & 2\tau_{xy} & 2\tau_{xy} \\ 0 & 0 & c^2 Re & c^2 Re \\ 1 & 0 & 0 & 0 \end{bmatrix}. \tag{35}$$

The eigenvectors form a basis for real $c \neq 0$, hence the system (equation 11) is hyperbolic. The structure of this system is particularly simple with two non-propagating components, whose physical significance will be addressed below. The multiplicity-two zero characteristic speed allows considerable analytical progress.

Consider a local linearization in which we use average values (denoted by an overbar) in the eigenvector expressions

$$\overline{R}=\begin{bmatrix} 0 & 0 & -\overline{c} & \overline{c} \\ 0 & 1 & 2\overline{\tau}_{xy} & 2\overline{\tau}_{xy} \\ 0 & 0 & \overline{c}^2 \mathrm{Re} & \overline{c}^2 \mathrm{Re} \\ 1 & 0 & 0 & 0 \end{bmatrix}, \quad \overline{R}^{-1}=\frac{1}{2\overline{c}^2}\begin{bmatrix} 0 & 0 & 0 & 2\overline{c}^2 \\ 0 & 2\overline{c}^2 & -4\overline{\tau}_{xy}/Re & 0 \\ -\overline{c} & 0 & 1/Re & 0 \\ \overline{c} & 0 & 1/Re & 0 \end{bmatrix}.$$

The characteristic variables of the problem are

$$w=\begin{bmatrix} w_1 \\ w_1 \\ w_3 \\ w_4 \end{bmatrix}=\overline{R}^{-1} q=\begin{bmatrix} \tau_{yy} \\ \tau_{xx}-2\overline{\tau}_{xy}/\left(\overline{c}^2 Re\right)\tau_{xy} \\ -v_x/2\overline{c}+\tau_{xy}/\left(2\overline{c}^2 Re\right) \\ v_x/2\overline{c}+\tau_{xy}/\left(2\overline{c}^2 Re\right) \end{bmatrix},$$

and (equation 11) can be rewritten in terms of these variables as

$$\frac{\partial w}{\partial t}+\Lambda\frac{\partial w}{\partial y}=\varphi, \tag{36}$$

with $\mathbf{\Lambda} = diag\ \{\mu_1,\mu_2, \mu_3,\mu_4\}$ and $\varphi = \boldsymbol{R}^{-1}\psi$,

$$\varphi = -\frac{1}{\lambda}\begin{bmatrix} \tau_{yy} + a\left(\tau_{xy}^2 + \tau_{yy}^2\right) \\ \tau_{xx} + a\left(\tau_{xy}^2 + \tau_{xx}^2\right) - 4\overline{\tau}_{xy}\,\sigma \\ \sigma \\ \sigma \end{bmatrix},\quad \sigma = \frac{\tau_{xy}}{2\overline{c}^2 Re}\left(1 + a\left(\tau_{xx} + \tau_{xx}\right)\right).$$

The forcing term φ can be rewritten as a function of the characteristic variables $\varphi = \varphi(w)$ by using the transformation,

$$q = \overline{R}w = \begin{bmatrix} \overline{c}\,(w_4 - w_3) \\ w_2 + 2\overline{\tau}_{xy}\,(w_3 + w_4) \\ \overline{c}^2\,(w_3 + w_4)\,Re \\ w_1 \end{bmatrix}. \tag{37}$$

3.3.2 Characteristic boundary conditions—The hyperbolic structure of the problem indicates the compatible physical boundary conditions that must be used in numerical simulations. The non-propagating quantities $w_1 = \tau_{yy}$ and $w_2 = \tau_{xx} - \frac{2\overline{\tau}_{xy}}{\rho\overline{c}^2}\tau_{xy}$ can be freely specified initially on the bottom and top boundaries. Subsequent values must be determined by solving the ordinary differential equations at each boundary

$$\begin{aligned} \frac{\partial w_1}{\partial t} &= -\frac{1}{\lambda}\left[\tau_{yy} + a\left(\tau_{xy}^2 + \tau_{yy}^2\right)\right], \\ \frac{\partial w_2}{\partial t} &= -\frac{1}{\lambda}\left[\tau_{xx} + a\left(\tau_{xy}^2 + \tau_{xx}^2\right) - 4\overline{\tau}_{xy}\,\sigma\right]. \end{aligned} \tag{38}$$

At the lower plate ($y = 0$) only the $w_4 = -\frac{1}{2\overline{c}}v_x + \frac{1}{2\rho\overline{c}^2}\tau_{xy}$ quantity can be specified as a boundary condition since it is propagating into the fluid from the adjacent domain. The quantity $w_3 = -\frac{1}{2\overline{c}}v_x + \frac{1}{2\rho\overline{c}^2}\tau_{xy}$ propagates from within the fluid domain towards the boundary and must be determined as part of the solution procedure. Conversely, at the top boundary ($y = H$) w_3 can be given as a boundary condition and w_4 results from the solution procedure. Typically, we wish to give boundary conditions in terms of the physical variables. The essence of the above discussion is that we cannot impose *both* v_x and τ_{xy} at boundaries. We list common cases of compatible boundary conditions which inform experimental protocols for this class of models to be applicable.

1. *Velocity and normal stresses.* At the lower plate we specify v_x and propagation from within the channel as specified by the characteristic equation

$$\frac{\partial w_3}{\partial t} - c\frac{\partial w_3}{\partial y} = -\sigma/\lambda, \tag{39}$$

gives w_3. This allows $\tau_{xy} = 2\,\mathrm{Re}\,c^2\left(w_3 + \frac{1}{2\overline{c}}v_x\right)$ to be computed. We solve (equation 38) to obtain w_1, w_2. Using (equation 37) we then compute τ_{xx}, τ_{yy} thereby obtaining all the variables within the q vector. At the upper plate we proceed analogously, by

specifying v_x but obtaining τ_{xy} from the w_4 component as $\tau_{xy}=2\,Re\,c^2\left(w_4-\frac{1}{2c}v_x\right)$. The w_4 component is determined from propagation within the fluid by solving

$$\frac{\partial w_4}{\partial t}+c\frac{\partial w_4}{\partial y}=-\sigma/\lambda. \tag{40}$$

2. *Tangential and normal stresses*. At both boundaries we specify τ_{xy}. Solving (equation 38) gives w_1, w_2 and hence τ_{yy}, τ_{xx}. At the bottom boundary v_x is obtained from the propagating w_3 component by solving (equation 39) and at the top from the w_4 component obtained by solving (equation 40).
3. *Non-reflective top boundary condition*. To simulate an infinite domain we can set the incoming characteristic at $y = H \gg 1$ to zero, $w_3 = 0$. Numerically, care must be taken so there are no spurious reflections of the w_4 component at the $y = H$ boundary.

Figure 3 gives a graphical overview of the procedure used to set boundary conditions.

3.3.3 Upper convected Maxwell (UCM) solution—After the general analysis presented above let us consider an exactly solvable case. For the UCM model we have $a = 0$ and the system (equation 11) becomes

$$\begin{cases} \frac{\partial v_x}{\partial t}-\frac{1}{Re}\frac{\partial \tau_{xy}}{\partial y}=0 \\ \frac{\partial \tau_{xx}}{\partial y}-2\tau_{xy}\frac{\partial v_x}{\partial y}=-\frac{1}{\lambda}\tau_{xx} \\ \frac{\partial \tau_{xy}}{\partial t}-\left(\frac{\eta_p}{\lambda}+\tau_{yy}\right)\frac{\partial v_x}{\partial y}=-\frac{1}{\lambda}\tau_{xy} \\ \frac{\partial \tau_{yy}}{\partial t}=-\frac{1}{\lambda}\tau_{yy} \end{cases} \tag{41}$$

with an immediate solution for $\tau_{yy}(y, t) = \tau_{yy}(y, 0)\exp(-t/\lambda)$.

Assume that $\tau_{yy}(y, 0) = 0$, either because this is the true initial state of the system or that enough time has passed since an initial excitation to ensure the decay term $\exp(-t/\lambda)$ has become negligibly small. At later times, $\tau_{yy}(y, t) = 0$. Consequently the shear wave propagation velocity is constant $c=\sqrt{\eta_p/(\lambda Re)}$ and the above system (equation 41) decouples into a 2×2 linear system for v_x, τ_{xy},

$$\begin{cases} \frac{\partial v_x}{\partial t}-\frac{1}{\mathrm{Re}}\frac{\partial \tau_{xy}}{\partial y}=0 \\ \frac{\partial \tau_{xy}}{\partial t}-\frac{\eta_p}{\lambda}\frac{\partial v_x}{\partial y}=-\frac{1}{\lambda}\tau_{xy} \end{cases}, \tag{42}$$

and a linear equation for τ_{xx},

$$\frac{\partial \tau_{xx}}{\partial t}+\frac{1}{\lambda}\tau_{xx}=-2\tau_{xy}\frac{\partial v_x}{\partial y}. \tag{43}$$

The system (equation 42) describes the propagation of shear waves and is identical to the telegraphers equation (8) derived earlier in the linear Maxwell limit. The shear wave propagates

and decays as in the linear model. The convective nonlinearity of the UCM system appears as a source driving the τ_{xx} stress which in the linear model is zero. For known $v_x(y, t)$, $\tau_{xy}(y, t)$ the solution is

$$\tau_{xx}(y,t) = -2\int_0^t e^{-(t-t\prime)/\lambda}\tau_{xy}(y,t\prime)\frac{\partial v_x}{\partial y}(y,t\prime)\,dt\prime. \tag{44}$$

Longitudinal momentum is lost when τ_{xy} and $\partial v_x/\partial y$ are in phase, and gained when they are of opposite phase.

The telegraphers equation has been studied by a number of authors under various boundary conditions. In the Rayleigh (or first Stokes) problem the fluid in a half plane is set into motion by an impulsively started lower plate. The first published solution for an elastic Maxwell fluid was given by Carslaw and Jaeger [3] using Laplace transform methods. Laplace transform methods have also been applied by Kazakia & Rivlin [15], [25],[26]. Tanner [28], [29] considers a viscous Oldroyd-B fluid. Narain & Joseph [23] present a boundary layer analysis of the problem. Joseph et al. [13], [12] consider perturbations of the plane Couette solution to account for a cylindrical rheometer. Preziosi & Joseph consider a generalization of Boltzmann's equation of linear viscoelasticity[24]. Denn & Porteus [5] consider reflections in startup flow associated with finite-depth effects.

The Stokes second problem, in which the lower plate undergoes harmonic oscillations, has received less attention. The Laplace transform method which has dominated most previous research cannot be applied when finite-depth effects are present and even in the half-plane case is unwieldy because of the continuous excitation of the fluid by the oscillating lower plate. To our knowledge the Riemann method [10] has not been applied to this problem as is done here, though it is a standard procedure for hyperbolic problems. The change of dependent variable

$$v_x(y,t) = \frac{1}{2}e^{-t/(2\lambda)}u(y,t), \tag{45}$$

transforms the telegraphers equation into a Klein-Gordon equation

$$\frac{\partial^2 u}{\partial t^2} - \frac{\partial^2 u}{\partial y^2} - \frac{u}{4\lambda^2} = 0. \tag{46}$$

In the characteristic variables $\xi = (ct - y)/4\lambda c$, $\eta = (y + ct)/4\lambda c$ the KIein-Gordon equation admits the Green function

$$G(\xi,\eta;\xi_Q,\eta_Q) = J_0(2\sqrt{(\xi_Q - \xi)(\eta_Q - \eta)}), \tag{47}$$

with J_0 the Bessel function of the first kind. This leads to the solution

$$\begin{gathered} u(y,t)=\frac{U(y-ct)+U(y+ct)}{2}+ \\ \int_{y-ct}^{y+ct}\left[K(s,y,t)\,U(s)+L(s,y,t)\,V(s)\right]\,ds, \\ K(s,y,t)=-\frac{t}{8\lambda^2 c}\frac{J_1(r(s,y,t))}{r(s,y,t)},\ L(s,y,t)=\frac{1}{2c}J_0(r(s,y,t)), \\ r(s,y,t)=\frac{1}{2\lambda c}\sqrt{(y+ct-s)(s-y+ct)}. \end{gathered} \tag{48}$$

Note that the kernel $K(s, y, t)$ in the integrand is nonsingular since

$$\lim_{s\to y\pm ct}K(s,y,t)=-\frac{t}{16\lambda^2 c}. \tag{49}$$

In the above, the initial value functions $U(y) = u(y, 0)$, $V(y) = u_t(y, 0)$, $u_t = \partial u/\partial t$, have been introduced. For $y > 0$ we have $U(y) = 0$, $V(y) = 0$. The original problem has boundary conditions given by $v_x(0, t) = \sin t$ and $\lim_{y\to\infty} v_x(y, t) = 0$. Through the same Riemann representation the boundary conditions can be transformed into initial conditions for $y < 0$ by assuming $V(y) = 0$ and solving the Fredholm integral equation of the second kind

$$U(y)=\mu\int_y^0 M(s,y)\,U(s)\ \mathrm{d}s+F(y), \tag{50}$$

$$M(s,y)=-\frac{y}{\sqrt{y^2-s^2}}J_1\left(\frac{1}{2\lambda c}\sqrt{y^2-s^2}\right), \tag{51}$$

$$F(y)=-4e^{-y/(2\lambda c)}\sin\frac{y}{c},\ \mu=\frac{1}{2\lambda c}, \tag{52}$$

for $U(y)$. The solution to this integral equation for $c = 1$, $\lambda = 4$ is shown in Fig. 4. The solution exhibits exponential growth as $y \to -\infty$, which is to be expected since the initial condition at some $y < 0$ is attenuated by viscosity until it reaches the $y = 0$ boundary condition line. High accuracy is essential therefore in numerical solution of (equation 50), but this can be achieved by using a Nystrom method and Gauss-Lobatto quadrature (for details see [21]).

The comparison in Fig. 5 of the telegraphers equation solution (equation 48) to the Ferry half-plane solution (equation 22) (for $c = 1$, $\lambda = 4$), shows the expected behavior with an initially large start-up error followed by asymptotic convergence of the telegraphers equation solution to the Ferry solution (equation 22). The error between the two models can be characterized using (equation 24). The shear wave speed for the UCM model is c while that for the Ferry solution is $1/\beta$. Hence the relative error in shear wave speed is

$$\varepsilon_c=1-\frac{\sqrt{2\lambda}}{\sqrt{\lambda+\sqrt{\lambda^2+1}}}. \tag{53}$$

Note that the error is large for small λ, i.e. the shorter the elastic relaxation time (or, equivalently, the more rigid the medium), the greater the error. The spatial attenuation length is $1/\alpha$ for the Ferry model and $2\lambda c$ for the UCM model. The relative error in attenuation length is therefore

$$\varepsilon_\alpha = \frac{1}{\sqrt{2\lambda}\sqrt{\sqrt{1+\lambda^2}-\lambda}} - 1, \tag{54}$$

and again is larger for small λ. The very large error between the initial transient which is correctly captured by the telegraphers equation solution and that of the asymptotic in time Ferry solution is shown in Fig. 6.

As mentioned, the tangential stress τ_{xy} satisfies the same telegraphers equation. However the boundary values at $y = 0$ are not known initially. However, we have transformed the half-plane boundary value problem into an initial value problem on the entire y-axis, an approach which now pays dividends since we can apply the first equation in (equation 42) everywhere to obtain

$$\frac{\partial \tau_{xy}}{\partial y} = \frac{\mathrm{Re}}{2} e^{-t/(2\lambda)} \left(\frac{\partial u}{\partial t} - \frac{1}{2\lambda} u \right). \tag{55}$$

This is an ordinary differential equation along constant t lines and we know that $\tau_{xy}(y \to \infty, t) = 0$. Hence τ_{xy} can be computed as

$$\tau_{xy}(y,t) = \frac{\mathrm{Re}}{2} e^{-t/(2\lambda)} \int_{y+ct}^{y} \left[\frac{\partial u}{\partial t}(s,t) - \frac{1}{2\lambda} u(s,t) \right] \mathrm{ds}, \tag{56}$$

where we have taken into account that $u = 0$, $\partial u/\partial t = 0$ for $s > y + ct$. Comparisons of the UCM model τ_{xy} with those from the Ferry solution are shown in Fig. 7. Notice that the differences in τ_{xy} are much greater than those in v_x.

In conclusion we obtain an exact solution of the nonlinear UCM model expressed as a convolution integral. The solution explicitly captures the nonlinear phenomenon of normal stress generation in shear, which one computes independently from a linear evolution of the velocity and shear stress, uncoupled from the normal stresses. This behavior has experimental implications, in that nonlinear behavior *cannot be detected* by monitoring velocity or shear stress. In order to ascertain nonlinear behavior experimentally, the first normal stress difference, which reduces to τ_{xx}, has to be measured. To test the accuracy of the UCM model, those measurements can be compared to the model results. In the simulations below, we present normal stresses generated from the boundary-controlled plate motion; the model predicts bulk strain thresholds to reach a certain normal stress level for given UCM parameters.

4 High resolution numerical solution

4.1 Numerical algorithm

For the more general nonlinear constitutive laws of Giesekus type with shear-thinning ($a \neq 0$), closed-form solutions do not exist, so numerical methods are employed. A primary purpose of this study is to provide a basis for inverse characterization of nonlinear viscoelastic properties.

Hence it is desirable to minimize any artificial dissipation and dispersion that might arise in a numerical computation, which is the baseline for matching with experimental data through parameter fitting. For this purpose, we apply a high-resolution algorithm [17] for hyperbolic PDEs as implemented in the CLAWPACK [18] or BEARCLAW packages [22]. We present the salient points of the numerical method here for completeness. It is a finite volume, Godunov-type method in which the jumps between adjacent finite volume cell averages are propagated in accordance with local wave speeds. Consider an uniform discretization of the interval $[0, H]$ with step size h. The cell center coordinates are $y_j = (j - 1/2)h$ for $j = 1, 2, \ldots, m$, and the cell edge coordinates are $y_{j-1/2} = (j - 1)h$, $j = 1, 2, \ldots, m + 1$, with $h = H/m$.

The cell finite volume average is

$$\mathrm{Q}_j^n = \frac{1}{h}\int_{y_{j-1/2}}^{y_{j+1/2}} q(y, t^n)\ \mathrm{dy}.$$

The evolution equation (11) can be rewritten as

$$\mathrm{q}_t = (\mathcal{A}+\mathcal{B})\,\mathrm{q}, \mathcal{A} = -A(q)\frac{\partial}{\partial x}, \mathcal{B} = \psi(\mathrm{q}), \tag{57}$$

with $\mathcal{A}$ the convective operator and $\mathcal{B}$ the source term operator. Equation (57) is split into two stages using Strang splitting,

$$\mathrm{q}(t+\Delta t) = e^{(\mathcal{A}+\mathcal{B})\Delta t} q(t) \cong e^{\mathcal{B}\Delta t/2} e^{\mathcal{A}\Delta t} e^{\mathcal{B}\Delta t/2} q(t).$$

The source term operator part of the splitting is $\boldsymbol{q}_t = \mathcal{B}\boldsymbol{q}$, a system of ODE's which is advanced in time using a second-order Runge-Kutta scheme. For the convective part, we first represent jumps between adjacent cells as propagating waves. The jump at the $j - 1/2$ interface $\Delta Q^n_{j-1/2}$, is decomposed on the eigenbasis $\overline{R} = R((\mathrm{Q}^n_j + Q^n_{j-1})/2)$

$$\Delta \mathrm{Q}^n_{j-1/2} = \mathrm{Q}^n_j - Q^n_{j-1} = \sum_{l=3}^{4} \alpha^l_{j-1/2} \mathrm{r}^l_{j-1/2},$$
$$\mathcal{W}^l_{j-1/2} = \alpha^l_{j-1/2} r^l_{j-1/2},\ l = 3, 4,\ n_w = 2.$$

Note that only the r_3, r_4 eigenmodes from (equation 35) are propagating, hence $n_w = 2$ waves $\mathcal{W}^{3,4}_{j-1/2}$ are required. The α coefficients required are

$$\alpha^3_{j-1/2} = \frac{\Delta Q_{3,\,j-1/2}}{2\overline{c}^2_{j-1/2}\mathrm{Re}} - \frac{\Delta Q_{1,\,j-1/2}}{2\overline{c}^2_{j-1/2}}, \alpha^4_{j-1/2} = \frac{\Delta Q_{3,\,j-1/2}}{2\overline{c}^2_{j-1/2} Re} + \frac{\Delta Q_{1,\,j-1/2}}{2\overline{c}_{j-1/2}},$$

with Q_1, Q_3 the 1, 3 components of $\boldsymbol{Q}$. Cell average values are updated by

$$Q_j^{n+1}=Q_j^n-\frac{\Delta t}{h}\left(\mathcal{W}^4_{j-1/2}+\mathcal{W}^3_{j+1/2}\right),$$

along with second-order corrections (for complete details, see [17]). The method is adaptive and second order in space and time.

4.2 Validation

To ensure accuracy of the method, numerical convergence studies and comparisons with the known analytical results (equation 30), (equation 48) were carried out. A typical numerical convergence result is presented in Table 1. The overall scheme exhibits an asymptotic convergence rate of 1.6.

Turning now to comparisons with the previous analytical results, formula (equation 30) is valid for a linear viscoelastic fluid after transients have died out. For small values of the boundary-controlled bulk strain parameter γ, the numerical results obtained by solving the nonlinear system (equation 11) for $a = 0$ should be close to those from the linear case (equation 30). This is indeed verified computationally and validates the numerical approach. Fig. 8 shows velocity profiles for a layer of thickness $H = 16$, hence $\gamma = 1/16 \ll 1$. In order to make such a comparison the parameters of the linear model must be related to those of the nonlinear model. In the nonlinear UCM model one chooses a Reynolds number Re, a polymer viscosity η_p and the Deborah number λ. We obtain the $\delta=\sqrt{i\,Re/\eta*}$ parameter in the linear solution (equation 30) by using formulas (equation 21) to compute η', η''.

There is the possibility of a phase error due to transient effects. To allow for this the comparison should be made at $t \gg 1$. The time history of the velocity at the layer midpoint $y = H/2$ is shown in an inset on Fig. 8 for $\lambda = 1$, $Re = 1$. After roughly 20 lower plate cycles the velocity shows periodic behavior. A time slice of the $v_x(y)$ dependence is chosen ($t^n = 129.912$ in Fig. 8). To eliminate any remnant phase error due to transients, the time at which to evaluate v_x using (equation 30) is determined by solving the equation

$$\mathcal{I}m\left\{e^{it}\frac{\sinh\left[\delta(H-y_1)\right]}{\sinh\left(\delta H\right)}\right\}=\mathrm{v}_x^n(y_1) \tag{58}$$

with $\mathrm{v}_x^n(y_1)$ denoting the velocity determined in the numerical procedure at time t^n. The phase error goes to zero as time increases, but slowly. For the parameters above, the solution of (equation 58) is $t = 129.928 \cong t^n$. The error between the numerical solution and the analytical result is shown in an inset on Fig. 8.

4.3 Experiment design guidelines from numerical results

An important aspect in the design of an experiment for viscoelastic characterization is to ensure controllable boundary conditions and to qualitatively understand the variation of the flow variables across the channel height H under various boundary conditions. We now apply the numerical algorithm presented above to show the effect of some experimentally relevant boundary conditions. We investigate the problem of inverse viscoelastic characterization using the numerical algorithm in the following section. In order to assess the effect of boundary conditions, fluid parameters are kept constant at $H = 10$, $\eta_p = 1$, $\lambda = 4$, $Re = 1$, $a = 0$ and $\tau_{yy} = 0$. Results are presented in Fig. 9-10 by showing superimposed plots of $v_x(y, t_n)$, $\tau_{xx}(y, t_n)$, $\tau_{xy}(y, t_n)$ at times $t_n = n\Delta t$, $n = 0, 1, \ldots, 10$, $\Delta t = 0.8$. Also shown are subsequent time positions

of tracer beads initially placed at $X(y, 0) = 0$. Since $\tau_{yy} = 0$ in these simulations the normal stress difference is directly given by τ_{xx}, $N_1 = \tau_{xx} - \tau_{yy} = \tau_{xx}$.

Open-cell experiment—In an open-cell experimental setup the viscoelastic fluid is typically in contact with the surrounding air which is assumed to exert a negligible tangential stress upon the viscoelastic layer. The top boundary at $y = 0$ is assumed to be flat. Hence the boundary condition $\tau_{xy}(H, t) = 0$ is set. Results for are shown in Fig. 9. Note that the nonlinear interaction terms in the UCM model lead to large values of τ_{xx}, larger than those for τ_{xy} near the plate.

Stationary upper plate—A closed-cell experimental setup is advantageous in ensuring isolation of the sample and surrounding medium. Typical results are shown in Fig. 10 when the upper plate is kept at zero velocity $v_x(H, t) = 0$. An interesting observation is that the velocity and stress profiles are very similar to those obtained in the open-cell experiment. The main difference is the much smaller range of motion exhibited by tracer beads when the upper plate is stationary by comparison to the open-cell experimental setup. If signal-to-noise ratio of tracer bead positions becomes a concern at low strain thresholds, then the open-cell setup is preferable.

5 Implications for inverse viscoelastic characterization

The theoretical results presented above provide new formulas in the linear finite depth case, nonlinear UCM case, and accurate numerical simulation algorithms for the nonlinear finite depth case. Especially for experimental measurements involving small samples, in which of necessity the depth is comparable to shear wavelengths, it is crucial to employ the finite depth formulas deduced above rather than trying to fit to the infinite depth shear wave (equation 22). In subsequent work we shall use theses new tools to deduce viscoelastic parameters from bead tracking data in the presence of experimental noise. For this paper we want to illustrate the effects that would arise from attempting to fit measurements to inappropriate models even if there were no experimental error whatsoever.

Instead of experimentally measured data we shall use bead positions generated from numerical simulations of a specific viscoelastic model. The goal then is to infer linear and nonlinear viscoelastic properties from this “experimental data set”, and to assess the magnitude of errors made as well as the dominant source of error. Typically least-squares procedures are employed to fit measured bead trajectories to theoretical formulas in order to obtain the complex viscosity $\eta^*(\omega)$ (or complex shear modulus $G^*(\omega)$). We adopt this procedure to provide fair measurements of relative error.

If the same model is used both to generate the data and to carry out parameter fitting, then errors arise only from generation of model solutions or the numerical least-squares procedure. We use this as a check to ensure the procedure is accurate. Further errors in viscoelastic characterization arise if the data is fit to a different model, e.g. if the Ferry infinite depth formulas are used to characterize measurements made on a linear viscoelastic fluid in a finite-depth cell. We present errors that arise from finite depth and nonlinear effects.

One unusual feature of these effects in the present non-dimensional formulation is that there is no frequency dependence. This is because we have restricted attention to a single-mode Maxwell type fluid.

5.1 Finite depth effects, linear viscoelastic model

Consider a viscoelastic fluid of depth H set into motion from rest by harmonic oscillation of a lower plate and upon which is placed a stationary upper plate ($v_H = 0$). We wish to ascertain the error made in deriving viscoelastic parameters (η^* or G^*) by fitting observed velocity

profiles to the Ferry semi-infinite solution (equation 22), rather than the correct, finite-depth solution given in (equation 30). Consider the following best-case experimental scenario: measurements are made at a large number of points, say $m = 40$, across the fluid depth and at small time increments, $\Delta t = 2\pi/n$ (e.g. $n = 36$ measurements per plate oscillation period). The bead positions generated by the finite-depth solution (equation 30) with complex viscosity $\eta_H^* = \eta_H' - \eta_H''$ are used to construct a least-squares fit to the Ferry tracer bead position profile from whence another estimate of the complex viscosity $\eta_F^* = \eta_F' - i\eta_F''$ is obtained. The least squares sum is

$$S(\eta_F', \eta_F'') = \sum_{j=1}^{m}\sum_{k=1}^{n} e^2(y_j, t_n, \delta_F, \delta_H), \delta_F = \sqrt{i\,\mathrm{Re}/\eta_F^*}, \delta_H = \sqrt{i\,\mathrm{Re}/\eta_F^*},$$
$$e(y, t, H, \delta_F, \delta_H) = \int_0^t \mathcal{I}m\left\{e^{is}\left[e^{-\delta_F y} - \frac{\sinh[\delta_H (H-y)]}{\sinh(\delta_H H)}\right]\right\} \mathrm{d}s, \tag{59}$$

The error function $e(y, t, H, \delta_F, \delta_H)$ is presented in Fig. 11-13. As expected when H increases the bead position error decreases (Fig. 11). Recall the link between complex viscosity and Maxwell fluid parameters, $\eta' = \eta_p/(1 + \lambda^2)$, $\eta'' = \eta_p\lambda/(1 + \lambda^2)$. We can increase the magnitude of the complex viscosity η^* by increasing η_p and vary the phase of η^* by varying λ but setting $\eta_p = 1 + \lambda^2$ always. When the absolute value of the complex viscosity increases, the error increases and furthermore becomes quasi-linear over the depth (Fig. 12). This makes the identification of parameters ill conditioned. As the relaxation time of the fluid λ becomes larger, the magnitude of the error remains essentially the same (Fig. 13). At small λ the identification of η^* will be more difficult since there are fewer oscillations of the shear wave within the depth H (Fig. 13).

Plots of the error in identification of η^* as presented above are useful, but limited to single values of the complex viscosity. To obtain an overall picture of the error made in identification of viscoelastic parameters we introduce the complex mapping $\delta_F(\delta_H)$, $\delta_F: \mathbb{C} \rightarrow \mathbb{C}$. This provides a measurement of the error in fitting the true finite-depth solution to the semi-infinite Ferry solution, and can also serve to correct the Ferry δ_F value. It is preferable to use δ rather than the complex viscosity η^* for two reasons: 1. $\delta = \alpha + i\beta$ is directly related to experimentally measured quantities, the penetration depth $1/\alpha$ and the shear wavelength $2\pi/\beta$; 2. The inversion $\eta^* = i\,Re/\delta$ amplifies errors made when δ is small and hence relatively small errors in δ give large changes in η^*.

A useful technique, common in the studies of conformal mappings, is to present the $\delta_F(\delta_H)$ mapping as a deformation of the $\alpha_H = j\,\Delta\alpha$ =constant and $\beta_H = k\Delta\beta$ =constant lines (j, k are integers and $\Delta\alpha$, $\Delta\beta$ are the spacings with which we sample δ_H space). If no error is made, an initially Cartesian (α_H, β_H) grid would be transformed into itself identically. The deviation from a Cartesian map of the (α_F, β_F) lines serves as an indication of the error made in using the Ferry formula in the least squares fit to obtain the complex viscosity. To cover as wide of range of values as possible the mappings are presented in logarithmic coordinates. Typical results for $H = 2, 5$ are presented in figures 14, 15. The purely viscous case $\alpha = \beta = \sqrt{Re/2}$ is shown for reference. As expected errors decrease as α increases - the shear wave is more attenuated and the boundary condition at H has less influence. Note however that large values of α in bead tracking experiments imply small bead displacements, which are difficult to track. For smaller values of α the wavelength $2\pi/\beta$ is poorly identified. The region of poor identification is smaller for smaller H as expected.

For certain regions it is even possible to use the $\delta_F(\delta_H)$ mapping to correct an erroneous estimate made by fitting to the Ferry semi-infinite solution. This would be of interest in

reinterpreting archived experimental data. Fig. 16 shows a sequence of values obtained by fitting to the infinite depth formula and arrows to the correct values (α, β) for that particular fluid.

It is apparent that very large errors are made when trying to deduce viscoelastic parameters from bead tracking data if the fit is carried out on the infinite depth formula rather than the correct, finite depth model.

5.2 Onset on non-linear effects

We now consider how non-linear effects influence viscoelastic characterization. Velocity profiles for a viscoelastic fluid placed between an oscillatory lower plate and a stationary upper plate are generated by numerically solving system (equation 11). The numerically-generated velocity profiles contain non-linear effects from (equation 11). In order to quantify the onset of nonlinearity we shall do a least-squares fit of the numerical velocity data to the linear finite-depth formula (equation 30) to obtain the parameters (α, β) characterizing the shear wave. We present typical results of the fitting procedure, highlighting the role of the bulk strain $\gamma = 1/H$ and Giesekus parameter a which controls shear thinning. At low values of γ (e.g. $\gamma < 0.1$) the fitting procedure reproduces the numerical parameters used in the simulations – this was used to validate the least squares algorithm used.

Moderate bulk strain, UCM fluid ($\gamma = 0.25$, $a = 0$)—Results are presented in Fig. 17. At this moderate bulk strain value the fitting procedure works very well for small Deborah numbers λ ($\lambda \leq 1$). As the Deborah number is increased the results become markedly worse with errors in parameter identification greater than 100% at $\lambda = 16$.

Large bulk strain, UCM fluid ($\gamma = 0.5$, $a = 0$)—When the bulk strain is large, the fitting procedure fails at all values of λ (Fig. 18).

Moderate bulk strain, Giesekus fluid ($\gamma = 0.25$, $a = 0.5$)—For moderate bulk strains on a shear-thinning fluid we notice a systematic overestimate of α even while β is captured rather well (Fig. ??). This is the expected behavior. The penetration depth of wave propagating into the fluid $1/\alpha$ is underestimated by the linear viscoelastic model hence the α values are higher.

6 Conclusions

For purposes of inverse characterization experiments in low volume samples of biological fluids (such as pulmonary airway surface liquids, our motivation for this work), we have extended the Ferry shear wave analysis to include finite-depth within linear viscoelasticity, and then to include nonlinearity with constitutive laws of Maxwell type. The linear models are exactly solvable, allowing for an explicit measure of errors in the inverse characterization of a known viscoelastic material due solely to finite depth effects. At frequencies and bulk strains typical for conditions encountered by the airway surface liquid in the lung, errors in the recovery of storage and loss moduli are enormous when fitting to inappropriate theoretical models. For viscoelastic fluids that can safely be assumed to be behave linearly, fitting to the newly derived finite depth formula (equation 30), which accounts for counterpropagating shear waves and stress modes, is shown to work well. If the fluid behaves nonlinearly as controlled bulk strain from the driven plate is ramped up, either due to convective nonlinearity or shear thinning, then inverse recovery of viscoelastic parameters by fitting to the extended finite-depth linear formulas induce significant errors.

These modeling tools have been developed in context with a new device, a micro, parallel-plate rheometer, which allows both types of velocity controls on the opposing flat interface to

the driven plate. The present paper has illustrated recovery of linear and nonlinear viscoelastic parameters as well as predictions of onset of nonlinear effects at threshold values of the imposed strain from the driven plate. In a future article, we will apply these modeling tools to experiments on biological liquids.

Acknowledgments

This work originated with and has benefited from discussions with colleagues involved in the University of North Carolina *Virtual Lung Project*. The research effort was sponsored by NIH grant R01-HL077546-01A2, NIH/NIDA 5-T90-DA022857-02, NSF Research Training Grant DMS-0502266, NSF-DMS 0604891, and ARO 47089-MS-SR. The authors wish to thank the paper's referees and G. McKinley for suggesting several pertinent references.

References

1. Adler FT, Sawyer WM, Ferry JD. Propagation of transverse waves in viscoelastic media. J Appl Phys 1949;20:1036–1041.
2. Bird, RB.; Armstrong, RC.; Hassager, O. Dynamics of Polymeric Liquids, Fluid Mechanics. Vol. 1. Wiley; New York: 1987.
3. Carslaw, HS.; Jaeger, JC. Operational Methods in Applied Mathematics. Oxford University Press; 1947.
4. Crocker JC, Valentine MT, Weeks ER, Gisler T, Kaplan PD, Yodh AG, Wietz DA. Phys Rev Lett 2000;85:888. [PubMed: 10991424]
5. Denn MM, Porteus KC. Elastic effects in flow of viscoelastic liquids. Chem Eng J 1971;2:280–286.
6. Ferry JD. Studies of the mechanical properties of substances of high molecular weight I. A photoelastic method for study of transverse vibrations in gels. Rev Sci Inst 1941;12:79–82.
7. Ferry, JD. Viscoelastic Properties of Polymers. John Wiley; New York: 1980.
8. Ferry JD, Sawyer WM, Ashworth JN. Behavior of concentrated polymer solutions under periodic stresses. J Polym Sci 1947;2:593–611.
9. Gregory Forest M, Wang Qi. Dynamics of slender viscoelastic free jets. SIAM J Appl Math 1994;54:996–1032.
10. Garabedian, P. Partial Differential Equations. AMS/Chelsea Publications; 1998.
11. Hill DB, Lindley B, Forest MG, Mitran SM, Superfine R. Microrheology of DNA solutions from bead tracking of shear waves. UNC preprint. 2007
12. Joseph, DD. Fluid Dynamics of Viscoelastic Liquids. Springer-Verlag; New York: 1990.
13. Joseph DD, Narain A, Riccius O. Shear-wave speeds and elastic moduli for different liquids. Part 1. Theory. J Fluid Mech 1986;171:289–308.
14. Joseph DD, Narain A, Riccius O. Shear-wave speeds and elastic moduli for different liquids. Part 2. Experiments. J Fluid Mech 1986;171:309–338.
15. Kazakia JY, Rivlin RS. Run-up and spin-up in a viscoelastic fluid. I. Reol Acta 1981;20:111–127.
16. Larson, RG. Constitutive Equations for Polymer Melts and Solutions. Butterworths; Guildford, UK: 1988.
17. LeVeque RJ. Wave propagation algorithms for multi-dimensional hyperbolic systems. J Comp Phys 1997;131:327–353.
18. LeVeque, RJ. CLAWPACK - Conservation Law Package. http://www.amath.washington.edu/~claw
19. Mason TG, Weitz DA. Optical measurements of frequency-dependent linear viscoelastic moduli of complex fluids. Phys Rev Lett 1995;74:1250–1253. [PubMed: 10058972]
20. Matsui H, Randell S, Peretti S, Davis CW, Boucher RC. Coordinated clearance of periciliary liquid and mucus from airway surfaces. J Clin Invest 1998;102:1125–1131. [PubMed: 9739046]
21. Mitran SM. Highly accurate solutions of the non-linear one-dimensional viscoelastic shear wave problem for Giesekus type fluids. in preparation.
22. Mitran, S. BEARCLAW - A software frame-work multiphysics numerical simulation. http://www.amath.unc.edu/Faculty/mitran/bearclaw.html

23. Narain A, Joseph DD. Linearized dynamics for step jumps of velocity and displacement of shearing flows of a simple fluid. Rheol Acta 1982;21:228–250.
24. Preziosi L, Joseph DD. Stokes' first problem for viscoelastic fluids. J Non-Newt Fl Mech 1987;25:239–259.
25. Rivlin RS. Run-up and spin-up in a viscoelastic fluid. II. Reol Acta 1982;21:107–111.
26. Rivlin RS. Run-up and spin-up in a viscoelastic fluid. III. Reol Acta 1982;22:213–222.
27. Schlichting, H. Boundary Layer Theory. McGraw-Hill; New York: 1960.
28. Tanner RI. Note on the Rayleigh problem for a visco-elastic fluid. Z angew Math Phys 1962;13:573–580.
29. Tanner, RI. Engineering Rheology. Oxford University Press; 2000.
30. Thurston GB, Schrag JL. Shear wave propagation in a birefringent viscoelastic medium. J Appl Phys 1964;35:144.
31. The UNC Virtual Lung Project. http://www.cs.unc.edu/Research/nano/vl/vlindex.html

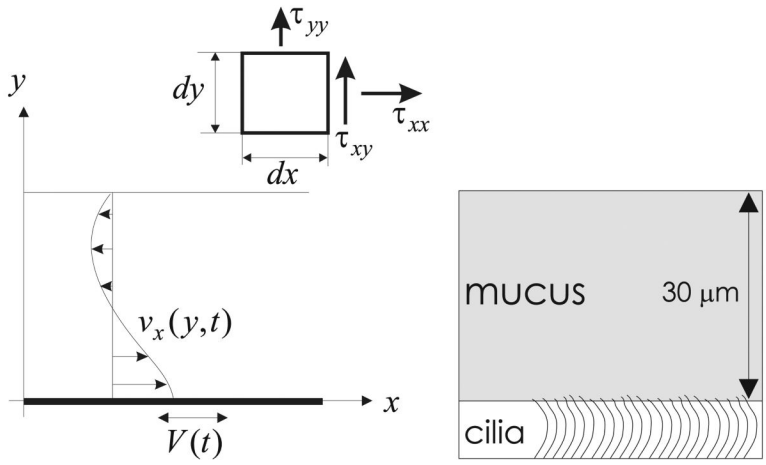

Figure 1.
Left: Schematic of oscillatory Couette flow and notation used to describe the deviatoric stress on an infinitesimal fluid element. The *x*-axis is parallel to the plate motion, the *y*-axis is the cross-channel direction. Right: Schematic of biological configuration in which multiple cilia impose an oscillatory motion on the bottom of a layer of viscoelastic fluid (e.g. mucus in pulmonary applications).

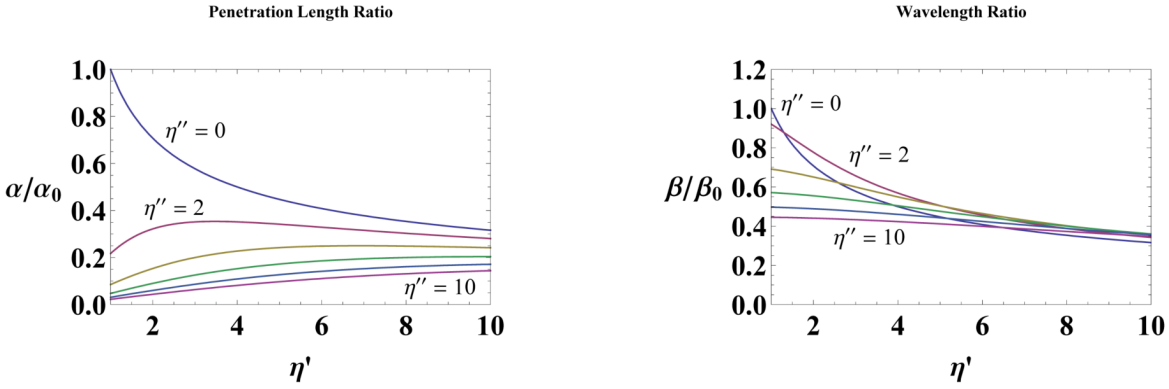

Figure 2.
Comparison of viscoelastic penetration ($1/\alpha$) and wave lengths ($2\pi/\beta$) to the viscous values ($1/\alpha_0$, $2\pi/\beta_0$)

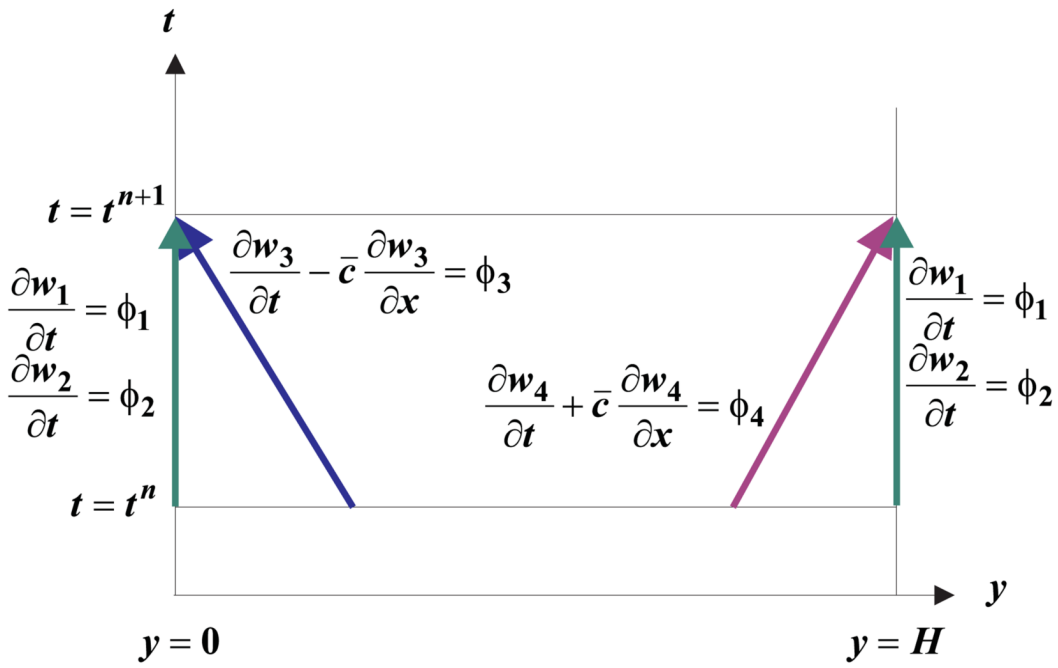

Figure 3.
Geometry of characteristics of system (equation 11) near the boundaries, highlighting characteristics coming from inside the computational domain (w_3 at $y = 0$, and w_4 at $y = H$) and non-propagating characteristic variables w_1, w_2.

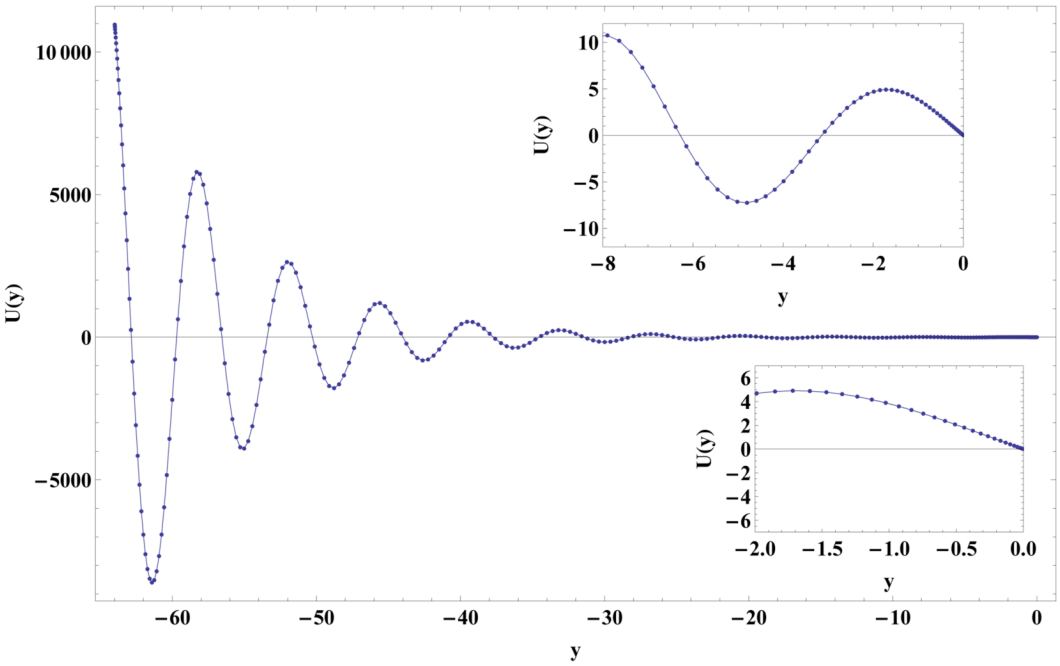

Figure 4.

Solution $U(y)$ to (equation 50) for $\lambda = 4$, $c = 1$. The solution gives initial values $U(y) = u(y, 0)$ obtained by transformation of boundary condition at $y = 0$, $u(0, t) = 2e^{t/(2\lambda)}\sin t$. A Nystrom method based upon Gauss-Lobatto qudrature with $n = 251$ nodes was used to discretize (equation 50). Exponential growth is observed for $y \to -\infty$. Insets show sharp resolution near the $y = 0$ boundary obtained by numerical method.

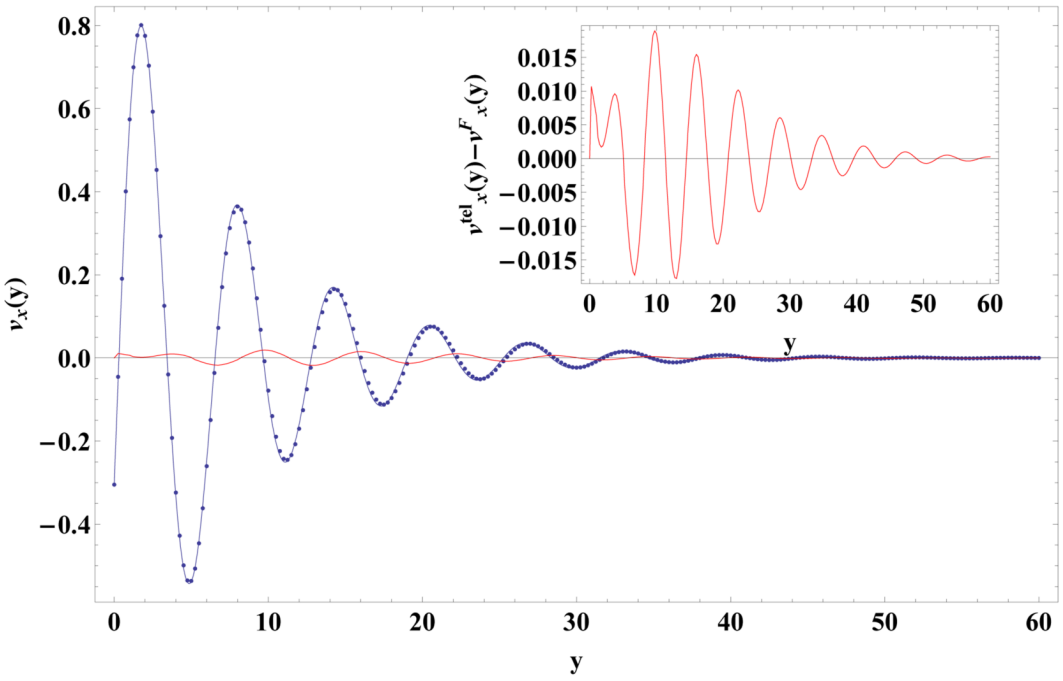

Figure 5.
Comparison at $t = 60$ of telgrapher's equation solution (48, dots) to Ferry solution (22, line) for $\lambda = 4$, $c = 1$. The inset shows the absolute error in the velocity $v_x(y, 60)$

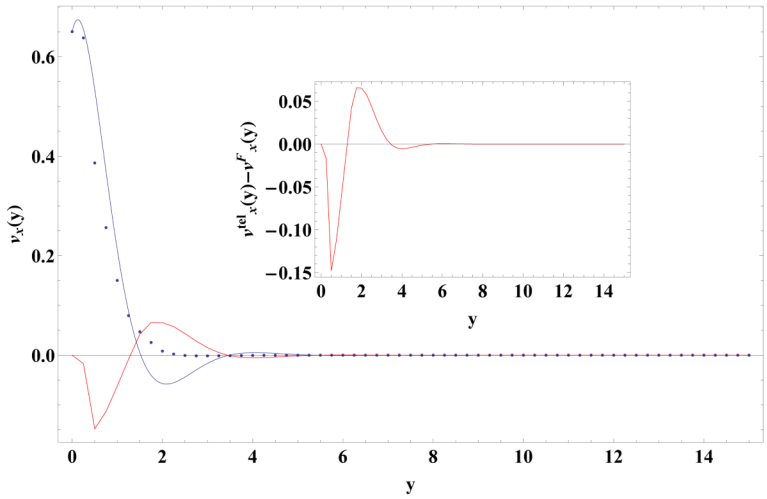

Figure 6.
As in Fig. 5 but for $c = 1$, $\lambda = 0.25$. At small λ the Ferry steady state solution exhibits very large errors with respect to the true initial transient.

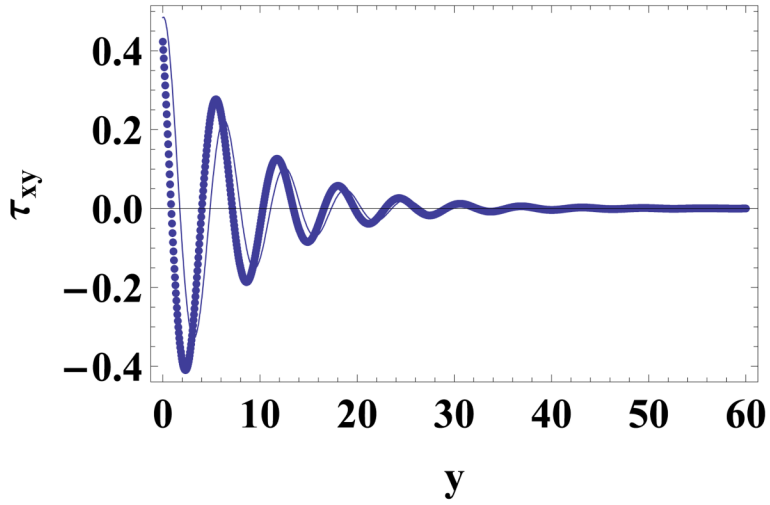

Figure 7.
Comparison of τ_{xy} from Ferry solution (28, line) with that from the telgrapher's equation solution (56, dots).

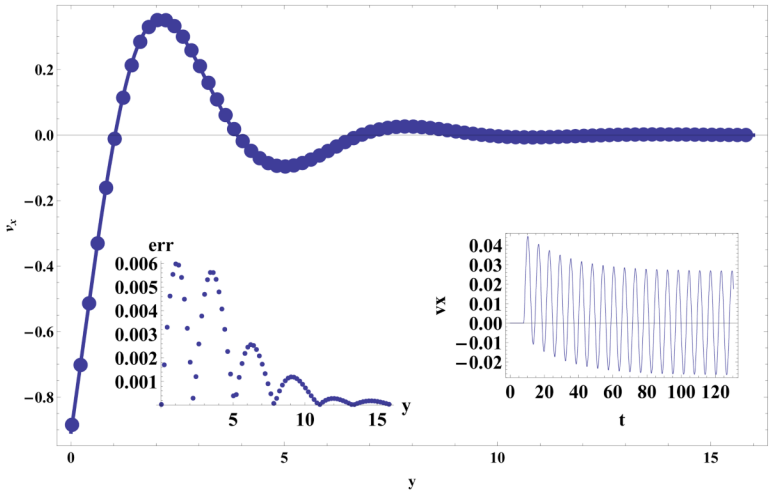

Figure 8.
Comparison of numerical result for $v_x(y, 130)$ (dots) to analytical prediction by (equation 30). Insets show absolute error at $t = 130$ and time history of $v_x(H/2, t)$ to indicate time needed for transients to pass.

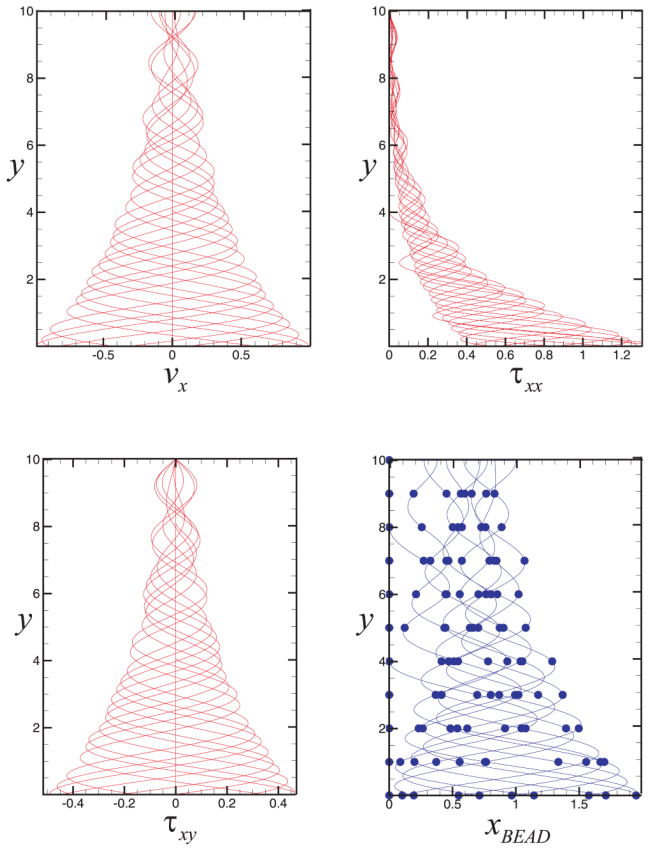

Figure 9.
Numerical results for zero top shear stress, $\tau_{xy}(H, t) = 0$, boundary condition.

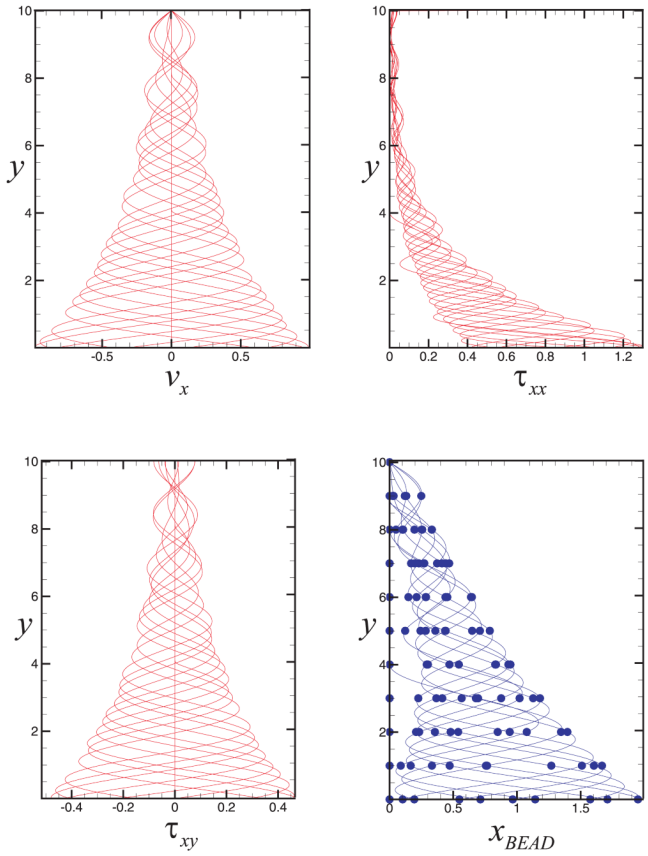

Figure 10.
Numerical results for stationary top plate boundary condition, $v_x(H, t) = 0$.

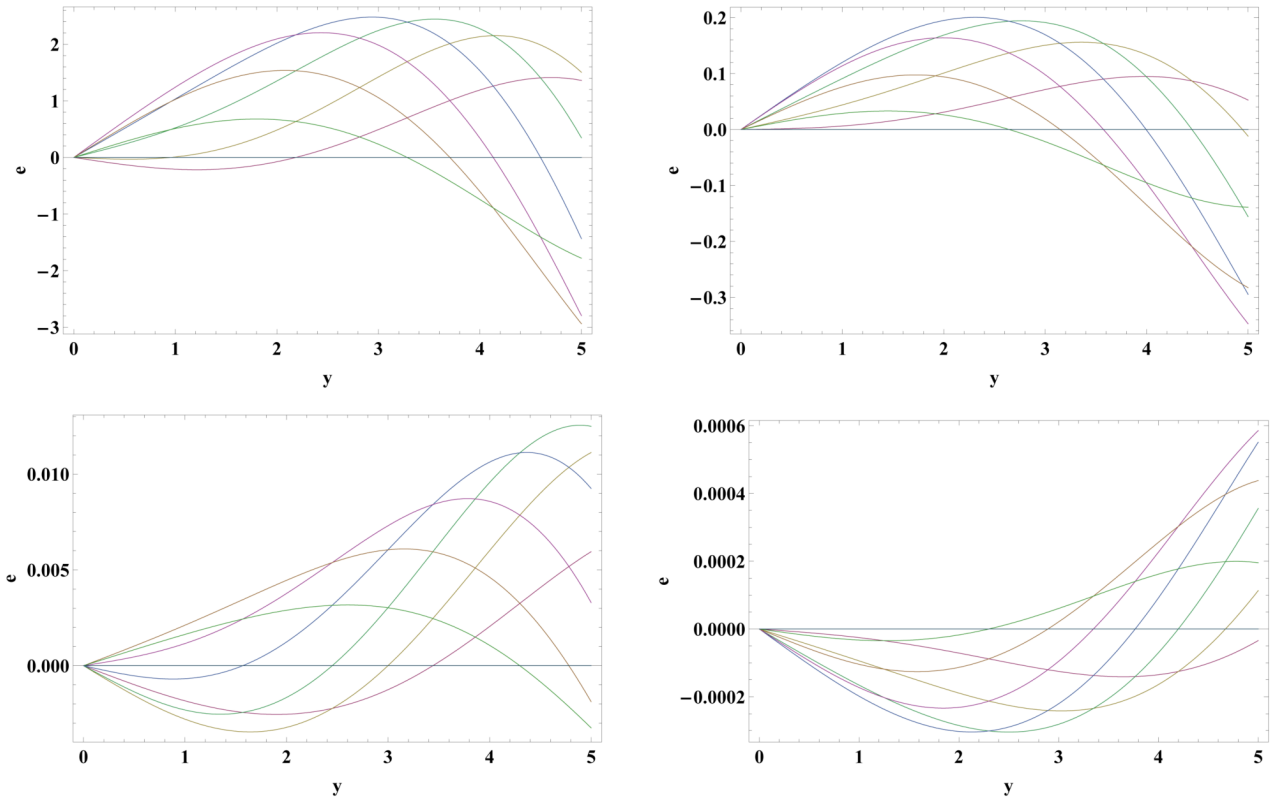

Figure 11.
Error in bead positions between finite depth (equation 30) and infinite depth (equation 22) solutions ($Re = 1$, $\eta' = \eta'' = 1$). Top row $H = 1, 5$. Bottom row $H = 10, 15$.

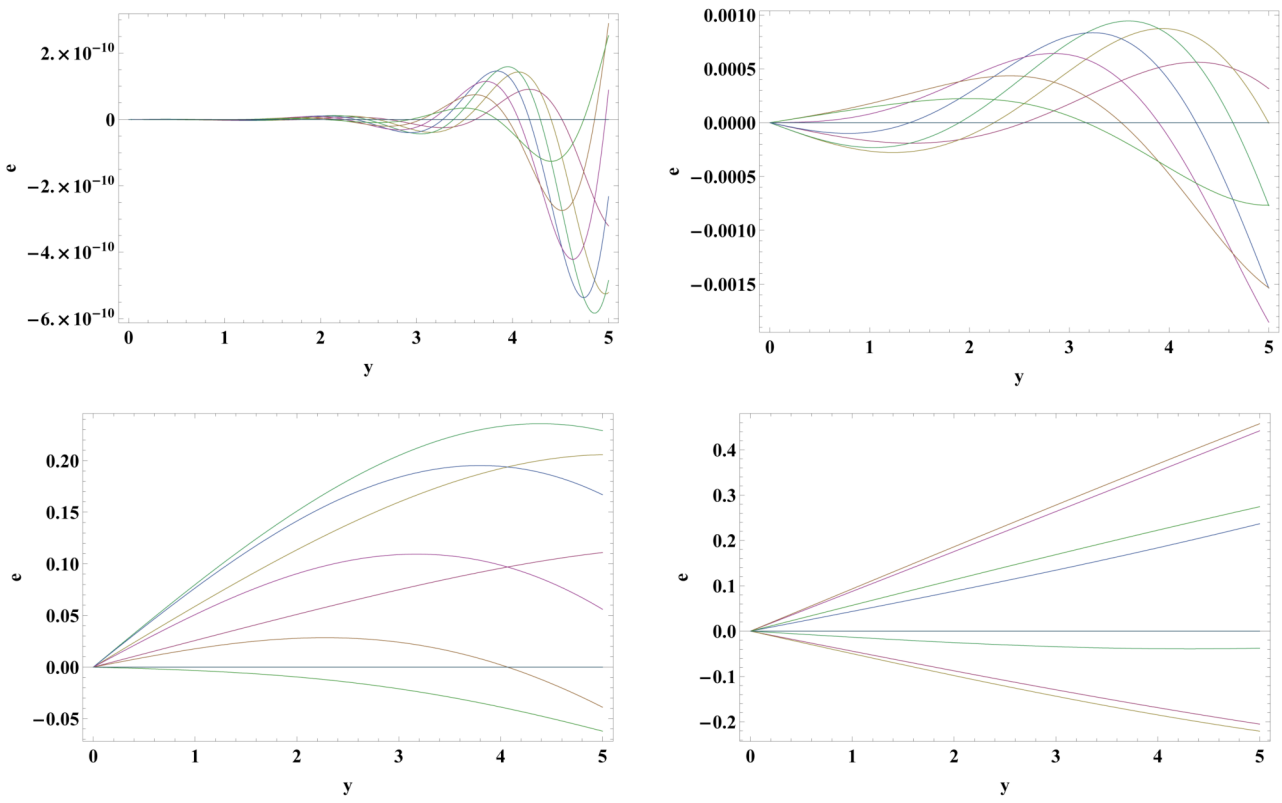

Figure 12.
As in Fig. 11. Constant $H = 10$. Top row $\eta' = \eta'' = 0.05, 0.5$. Bottom row $\eta' = \eta'' = 5, 50$.

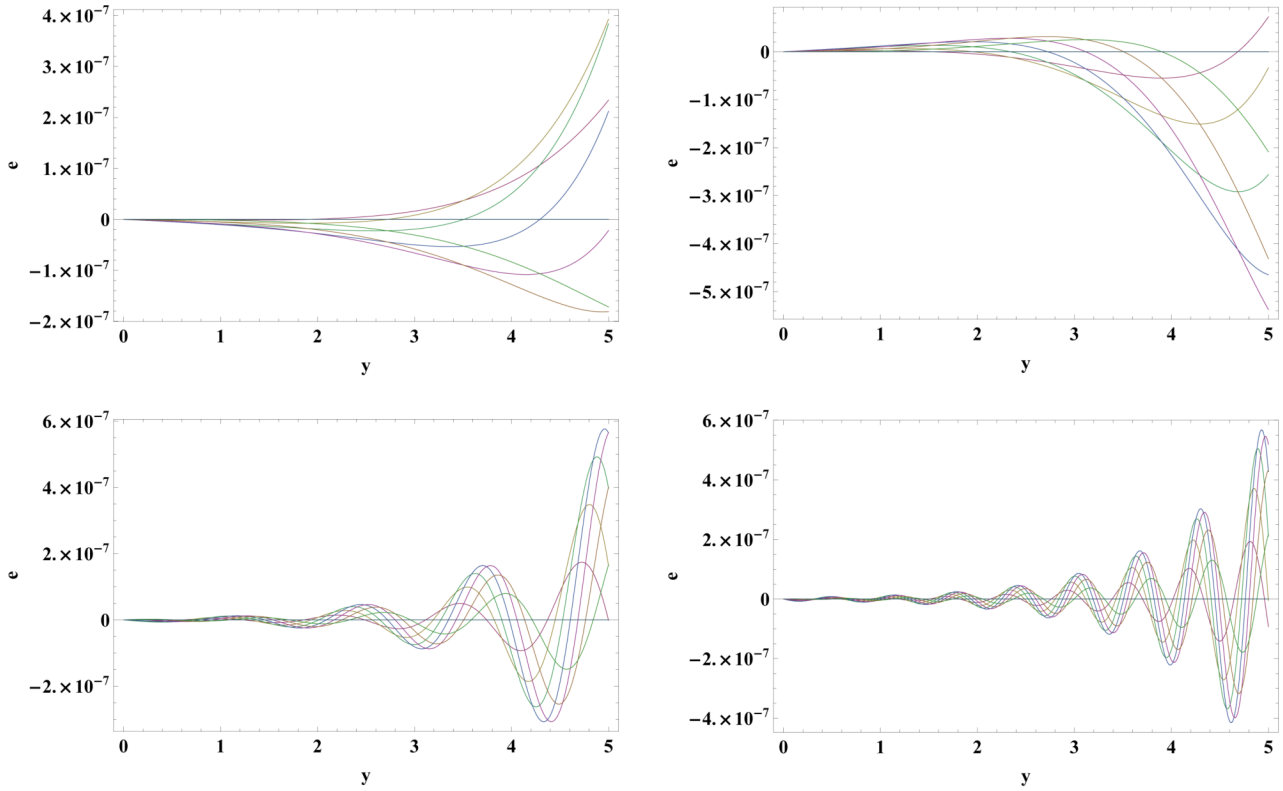

Figure 13.
As in Fig. 11. Constant $H = 10$. Top row $\lambda = 0.5, 1$. Bottom row $\lambda = 5, 10$. $\eta_p = 1 + \lambda^2$ in all cases.

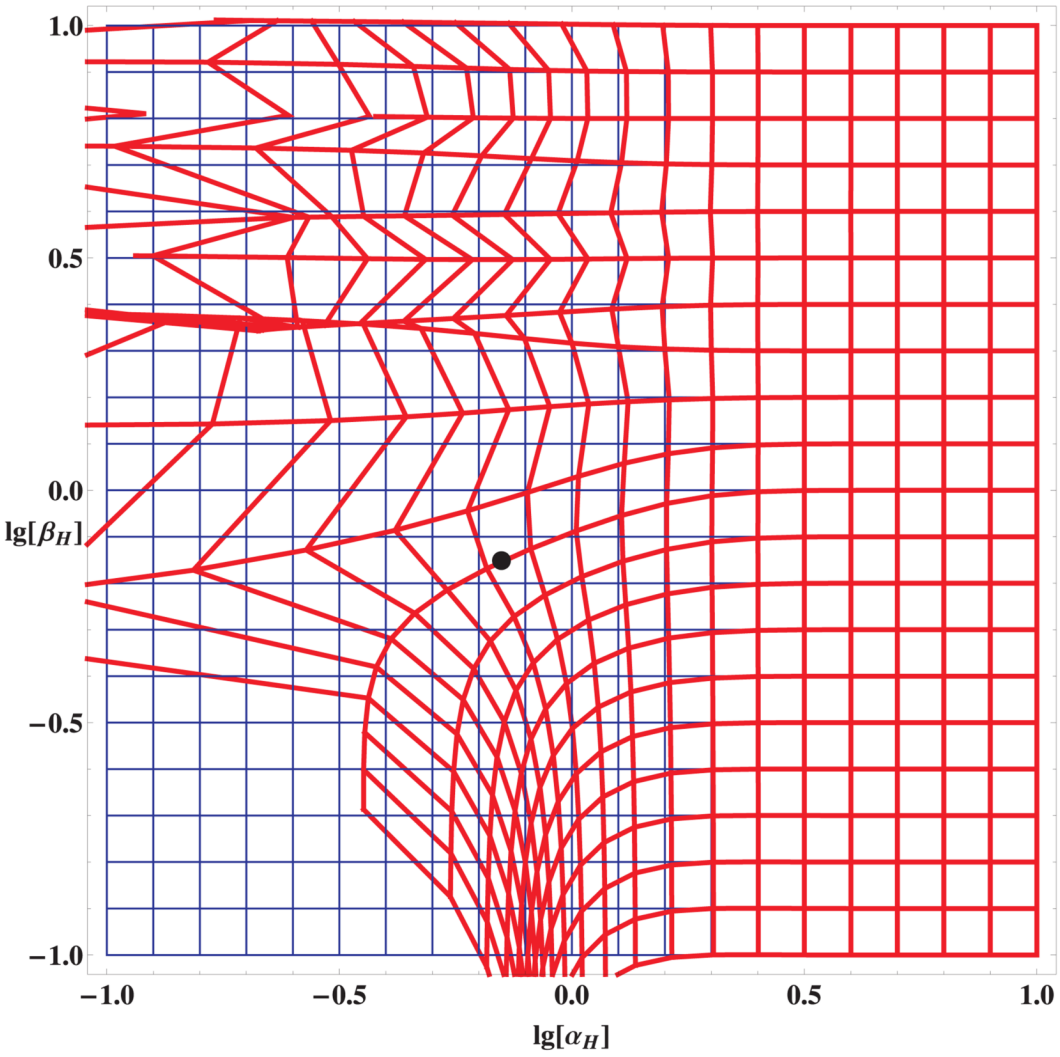

Figure 14.

The mapping δ_F (δ_H) for $H = 2$, $Re = 1$. The dot represents the purely viscous case $\alpha=\beta=\sqrt{1/2}$. Large errors in viscoelastic characterization arise for $\alpha < 10^{-0.25}$.

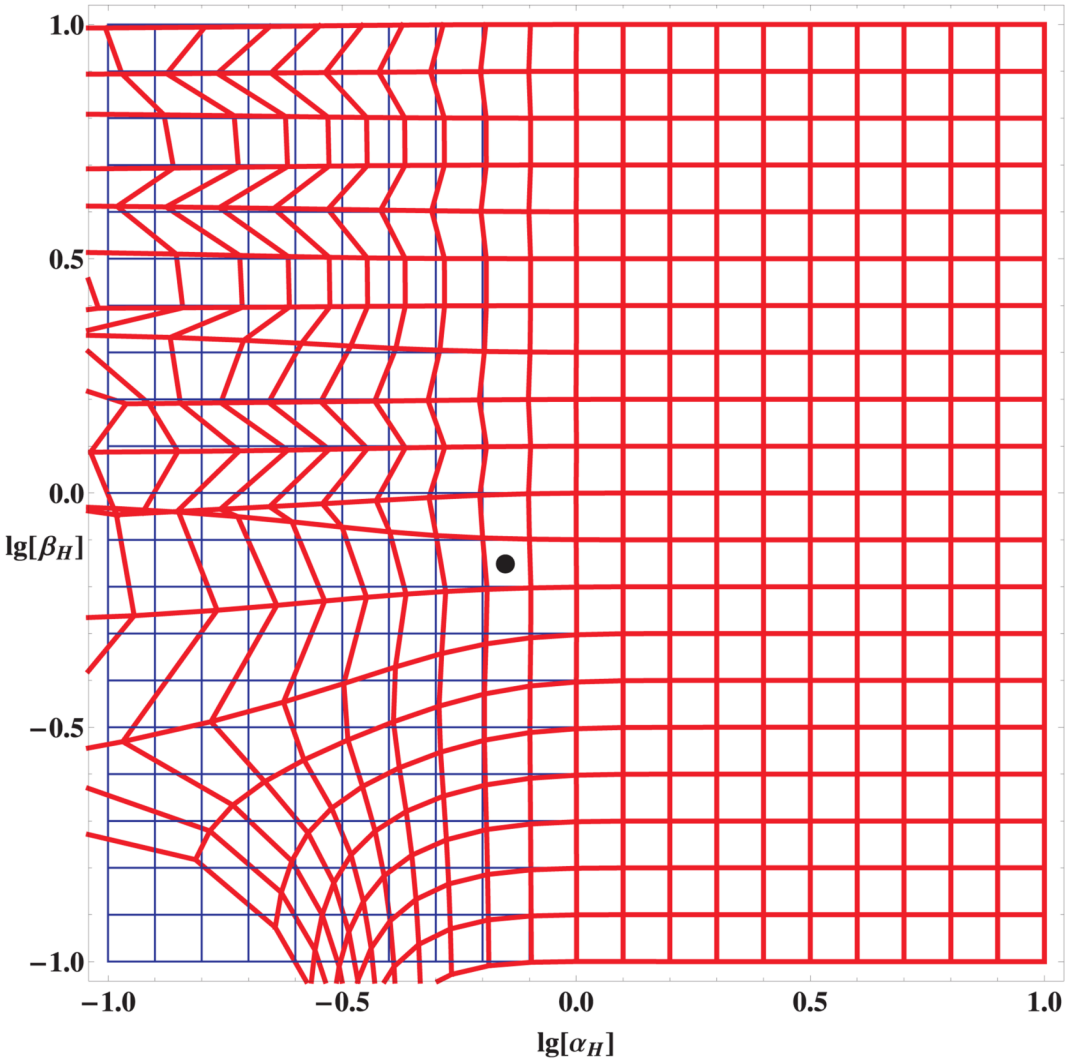

Figure 15.
As above for $H = 5$.

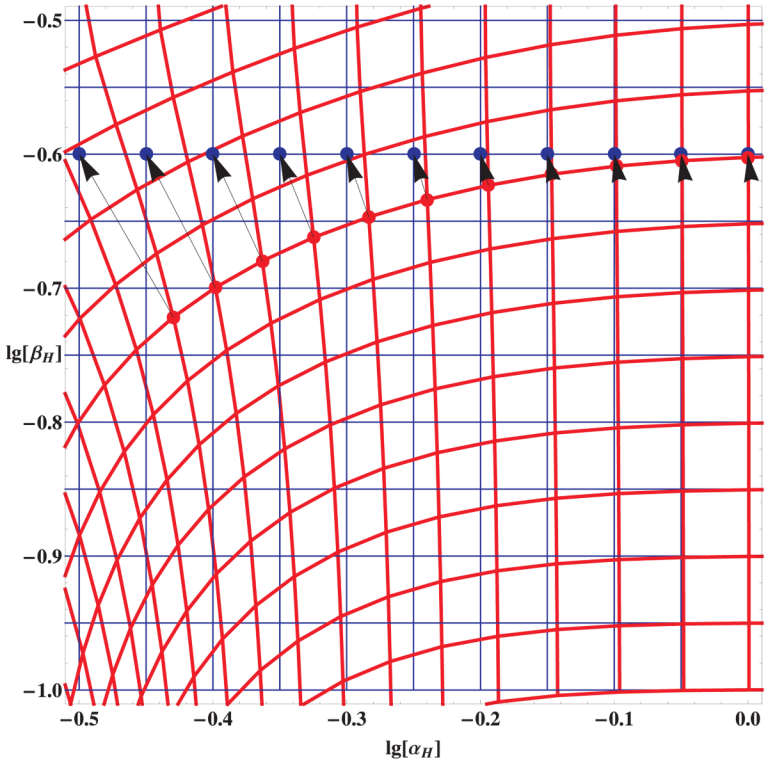

Figure 16.
A plot of δ_F (δ_H) for $H = 5$, $Re = 1$ with arrows indicating how to correct erroneous (α_F, β_F) values to the true viscoelastic fluid values (α_H, β_h), assuming linear viscoelasticity.

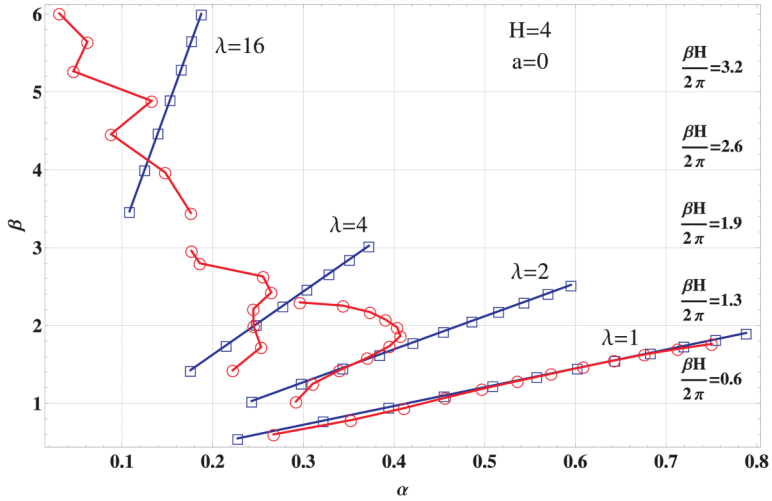

Figure 17.
Comparison of shear wave identified by fitting to the linear, finite depth formula (equation 30), (circles) to parameters used to generate data numericall (squares). Bulk strain $\gamma = 1/H = 0.25$.

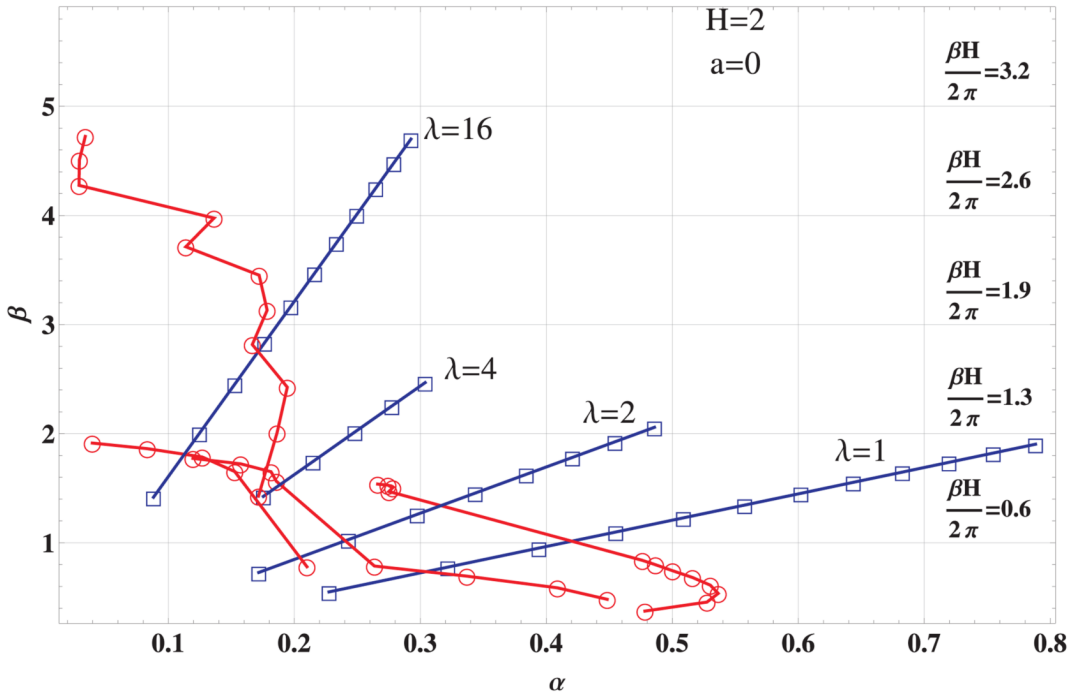

Figure 18.
As above, but for higher strain $\gamma = 1/H = 0.5$. Nonlinear effects are so strong that fitting to linear model leads to meaningless results.

Table 1

Numerical convergence results. The relative error ε is that in the velocity v_x at $y = H/2$ computed with m_y subintervals and at time $t = 12.96$. The exact solution is taken to be v_x computed with $m_y = 320$ subintervals. ($Re = 1$, $\lambda = 2$, $H = 1$, $V_H = 0$)

m_y	20	40	80	160
lg h	-1.30	-1.60	-1.90	-2.20
lg ε	-0.85	-1.20	-1.58	-2.06